Article

Cell Reports

# PDGF-B Is Required for Development of the Glymphatic System

## Graphical Abstract

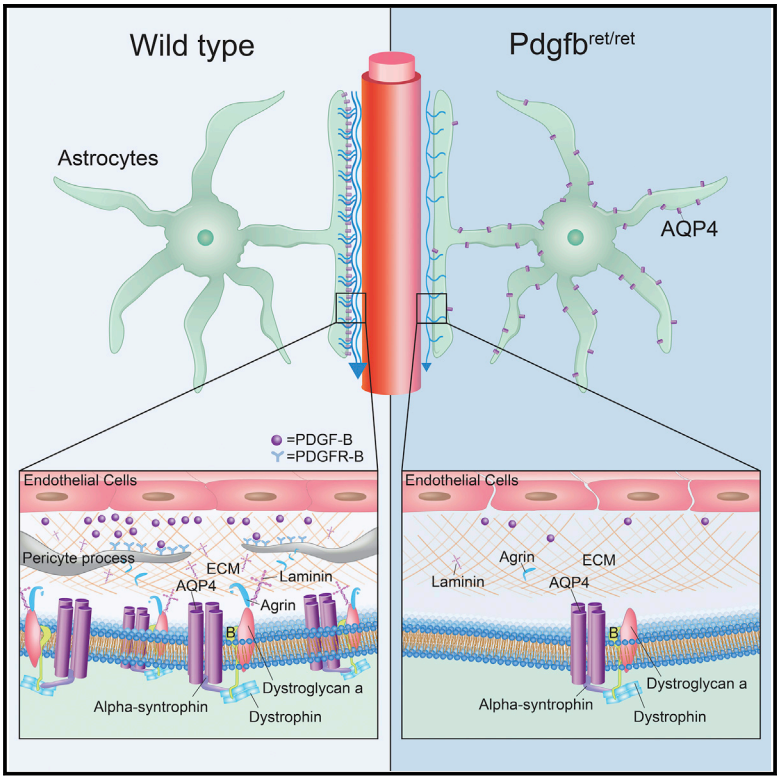


## Highlights

- The glymphatic system is first developed in the hippocampus
- Insufficient PDGF-B signaling decreases AQP4 polarization to astrocyte vascular endfeet
- Insufficient PDGF-B signaling impairs maturation of the glymphatic function

## Authors

Anne Sofie Munk, Wei Wang, Nicholas Burdon Bèchet, ..., Anja Meissner, Maiken Nedergaard, Iben Lundgaard

## Correspondence

iben.lundgaard@med.lu.se

## In Brief

Munk et al. unravel the developmental profile of the glia-lymphatic (glymphatic) system. Glymphatic function arises in the hippocampus at postnatal day 1 in conjunction with the polarized expression of AQP4 at astrocyte endfeet. PDGF-B signaling is implicated in normal glymphatic function, and reduced signaling reduces AQP4 polarization and glymphatic influx.

Munk et al., 2019, Cell Reports *26*, 2955–2969
March 12, 2019 
https://doi.org/10.1016/j.celrep.2019.02.050

CellPress

Cell Reports
Article



# PDGF-B Is Required for Development of the Glymphatic System

Anne Sofie Munk,[1,2,10] Wei Wang,[1,10] Nicholas Burdon Bèchet,[3,4,11] Ahmed M. Eltanahy,[3,4,5,11] Anne Xiaoan Cheng,[1,11] Björn Sigurdsson,[2] Abdellatif Benraiss,[1] Maarja A. Mäe,[6] Benjamin Travis Kress,[1,2] Douglas H. Kelley,[7] Christer Betsholtz,[6,8] Kjeld Møllgård,[9] Anja Meissner,[3,4] Maiken Nedergaard,[1,2] and Iben Lundgaard[1,3,4,12,*]
[1]Center for Translational Neuromedicine, University of Rochester, Rochester, NY 14642, USA
[2]Center for Basic and Translational Neuroscience, University of Copenhagen, 2200 Copenhagen, Denmark
[3]Department of Experimental Medical Science, Lund University, 221 84 Lund, Sweden
[4]Wallenberg Center for Molecular Medicine, Lund University, 221 84 Lund, Sweden
[5]Mansoura University Hospital, Faculty of Medicine, Mansoura University, 35516 Mansoura, Egypt
[6]Department of Immunology, Genetics and Pathology, Uppsala University, 751 85 Uppsala, Sweden
[7]Department of Mechanical Engineering, University of Rochester, Rochester, NY 14627, USA
[8]Integrated Cardio Metabolic Center (ICMC), Karolinska Institutet, Novum, 141 57 Huddinge, Sweden
[9]Department of Cellular and Molecular Medicine, University of Copenhagen, 2200 Copenhagen, Denmark
[10]These authors contributed equally
[11]These authors contributed equally
[12]Lead Contact
*Correspondence: iben.lundgaard@med.lu.se
https://doi.org/10.1016/j.celrep.2019.02.050

## SUMMARY

**The glymphatic system is a highly polarized cerebrospinal fluid (CSF) transport system that facilitates the clearance of neurotoxic molecules through a brain-wide network of perivascular pathways. Herein we have mapped the development of the glymphatic system in mice. Perivascular CSF transport first emerges in hippocampus in newborn mice, and a mature glymphatic system is established in the cortex at 2 weeks of age. Formation of astrocytic endfeet and polarized expression of aquaporin 4 (AQP4) consistently coincided with the appearance of perivascular CSF transport. Deficiency of platelet-derived growth factor B (PDGF-B) function in the PDGF retention motif knockout mouse line *Pdgfb*$^{ret/ret}$ suppressed the development of the glymphatic system, whose functions remained suppressed in adulthood compared with wild-type mice. These experiments map the natural development of the glymphatic system in mice and define a critical role of PDGF-B in the development of perivascular CSF transport.**

## INTRODUCTION

To maintain an optimal environment for neuronal signaling within the brain, waste products must be eliminated, and extracellular ionic concentrations and fluid levels efficiently regulated (Plog and Nedergaard, 2018). The glia-lymphatic (glymphatic) system removes solutes, such as lactate (Lundgaard et al., 2017), amyloid β (Aβ) (Iliff et al., 2012), and tau (Iliff et al., 2014), via perivascular transport in the CNS. Astrocytes extend vascular processes, the so-called endfeet, which ensheath 60%–90% of the cerebral vasculature (Korogod et al., 2015; Mathiisen et al., 2010; Nagelhus and Ottersen, 2013) and play an instrumental role in ion buffering and homeostasis (Schreiner et al., 2015). Glymphatic clearance is dependent on aquaporin-4 (AQP4) water channels located in astrocytic vascular endfeet (Nielsen et al., 1997) for exchange of solutes between the cerebrospinal fluid (CSF) and interstitial fluid (Iliff et al., 2012; Mestre et al., 2018).

Glymphatic function is perturbed in old age, and loss of glymphatic function in *Aqp4* knockout mice accelerates Aβ plaque formation and cognitive dysfunction in the APP/PS1 Alzheimer's disease mouse model (Xu et al., 2015), suggesting that lack of glymphatic function renders the brain susceptible to the accumulation of neurotoxic substances. The existence of a glymphatic system in human brain has been demonstrated by the brain-wide dispersion of contrast agent in CSF following intrathecal administration (Ringstad et al., 2018). Consistent with findings from animal studies, detailing approximately 10-fold higher glymphatic activity in the sleep state than the awake state (Xie et al., 2013), acute sleep deprivation increases the Aβ load in the human brain (Shokri-Kojori et al., 2018), thus substantiating a role for perivascular transport of solutes in the human brain. AQP4 polarization to vascular endfeet is used as a surrogate marker of glymphatic function, and loss of AQP4 polarization has been detected in Alzheimer's disease patients (Zeppenfeld et al., 2017), corroborating the findings of animal studies.

The anatomical pathways for the glymphatic system are the perivascular spaces, which at leptomeningeal vessels are fluid-filled spaces and in parenchymal vessels consisting of highly organized extracellular matrix, enriched in collagen IV and laminin, of which many are produced by pericytes (Bell et al., 2010; Vanlandewijck et al., 2018) and the specialized fibroblasts located within the brain's perivascular space (Vanlandewijck et al., 2018). We here hypothesize that PDGF-B signaling, crucial for the development of pericytes and vascular smooth muscle cells (Hellström et al., 1999; Lindahl et al., 1997), is crucial also

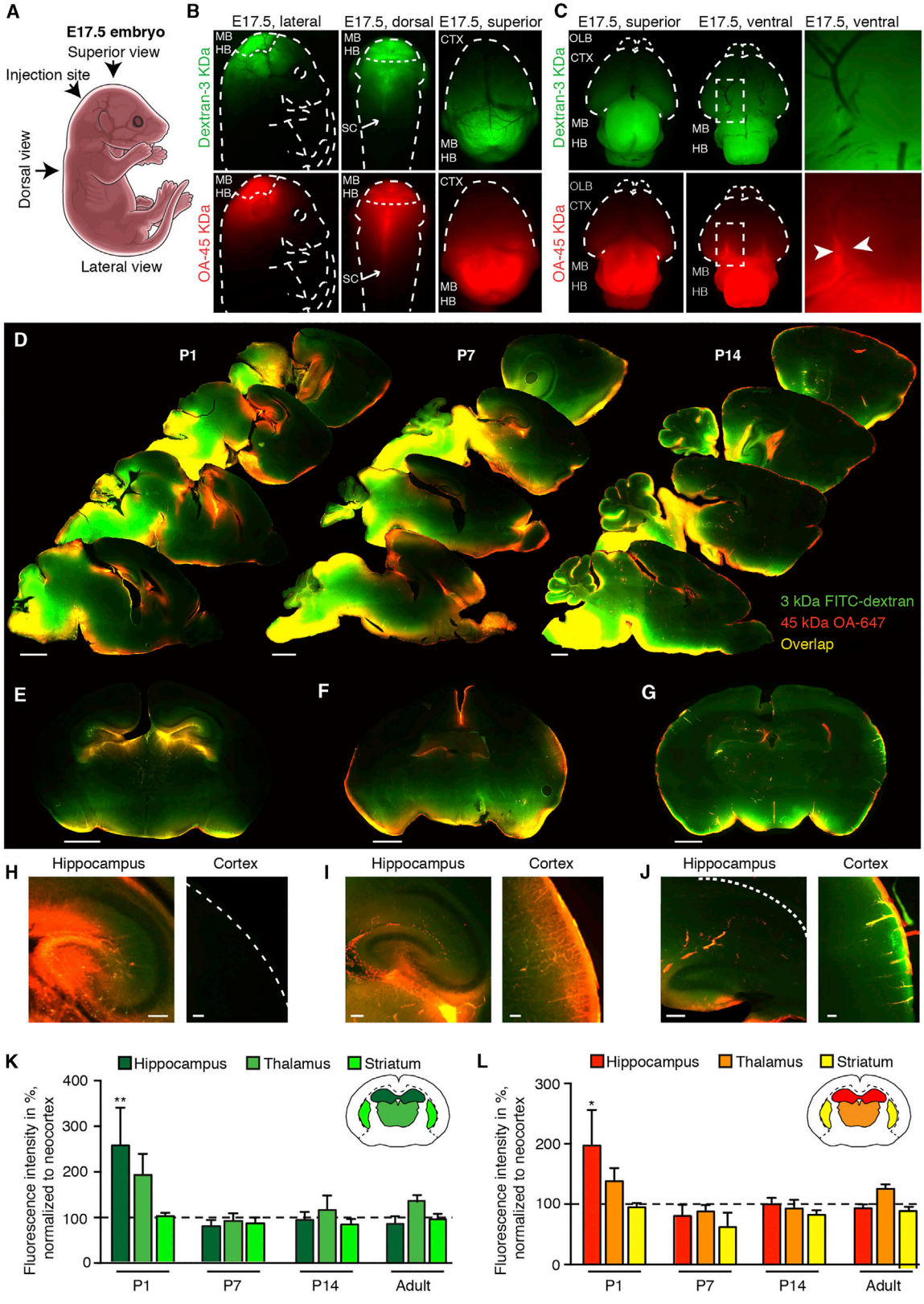


*(legend on next page)*

for glymphatic function because of its regulation of the perivascular environment. Pericytes may play an important role in blood-brain barrier (BBB) formation during development by inducing the expression of tight junction proteins by the endothelial cells, including zonula occludens-1 and occluding (Bell et al., 2010; Daneman et al., 2010), and thereby efficiently separating the perivascular space from the circulation. We used a developmental approach to understand how and when glymphatic function is established in mice. We found that glymphatic function depends on establishment of astrocyte endfeet and their polarized expression of AQP4 during development. We also report regional differences in the developmental profile of glymphatic fluid transport, with perivascular influx appearing first in the hippocampus in newborn mice. Using the platelet-derived growth factor B (PDGF-B) retention motif knockout mouse line *Pdgfb*$^{ret/ret}$ (Lindblom et al., 2003), a critical role of PDGF-B for glymphatic function was established. Reduction in PDGF-B availability was associated with pericyte deficiency, loss of AQP4 polarization, and suppression of glymphatic activity.

## RESULTS

### The Glymphatic System Is Not Developed in Embryonic Day 17.5 Embryos

To assess glymphatic function in E17.5 mice, CSF tracers (dextran-fluorescein isothiocyanate [FITC] [3 kDa] and ovalbumin [OA]-647 [45 kDa]) were slowly infused into the cisterna magna *in utero* (Figure 1A). The tracer sizes used here are not permeable to the BBB or CSF-meningeal barriers, which are present at this time point in development (Butt et al., 1990). Establishment of barriers at the subarachnoid CSF compartment happens by E14 through loss of fenestration in pial-arachnoid blood vessels (Balslev et al., 1997). The distribution of tracers in the embryonic brain resembled a pattern largely consistent with diffusion, with the greatest fluorescence intensity localized to regions in closer proximity to the site of infusion, primarily the mid- and hindbrain (Figures 1B and 1C). No CSF tracer movement was observed in the cortex of intact embryos (Figure 1B), whereas *ex vivo* imaging of the whole brains showed some accumulation of 45 kDa OA-647 tracer along the posterior communicating artery of the circle of Willis (Figure 1C). Perivascular distribution of tracer was absent in the dorsal and ventral cortex, apart from the partial distribution at circle of Willis.

### Regional Influx Patterns Differ through Development

We then assessed CSF accessibility to the brain at increasing postnatal ages by injecting CSF tracers into the cisterna magna compartment. Examination of the ventral aspect of whole postnatal day (P) 1 brains revealed perivascular tracer distribution along the posterior communicating artery, middle cerebral artery, and anterior cerebral artery in addition to the medial orbitofrontal arteries (Dorr et al., 2007), from which the larger tracer (45 kDa OA) reached the piriform cortex caudal to the olfactory bulb (Figure S1). In contrast, the smaller tracer (3 kDa dextran) exhibited only minimal perivascular association, possibly because of diffusion of the tracer directly into the penetrable, immature tissue with a 36%–46% extracellular space volume (Lehmenkühler et al., 1993). Perivascular influx ceased before the first branchpoint of the MCAs, and tracer was not visible in the dorsal parts of the cortex (Figure 1D). Interestingly, the hippocampus was the only area that exhibited tracer penetration into the parenchyma in newborn mice (Figures 1D, 1E, and 1H).

Imaging of the ventral side of P7 brains showed that the perivascular influx followed the basilar artery and the circle of Willis to the MCAs (Figure S1). Coronal brain slices exhibited a gradient of parenchymal tracer influx from piriform to insular to neocortex, with the highest intensity in the piriform cortex and very low tracer intensity in the most dorsal parts of the neocortex (Figures 1D and 1F). Robust CSF tracer intensity appeared in the olfactory bulb at P7, a major CSF clearance pathway (Mollanji et al., 2002) (Figure 1D). Thus, in 1-week-old mice, tracer influx resembled adult perivascular tracer distribution in hippocampus, piriform cortex, and olfactory bulb parts, but not the most dorsal parts, of the neocortex (Figures 1D and 1F). Robust tracer influx into the hippocampus persisted throughout all ages (Figures 1E and 1I). Surprisingly, perivascular influx in multiple brain regions, including dorsal cortex and thalamus, was first robustly developed at P14, at which point the pattern of tracer distribution resembled the pattern of tracer penetration in adult mice (Figures 1D, 1G, and 1J) (Iliff et al., 2012; Kress et al., 2014).

Quantifications of CSF penetration confirmed that there was twice as much CSF tracer in the hippocampus as the cortex in newborn mice (3 kDa dextran tracer, $p = 0.02$; 45 kDa OA tracer, $p = 0.015$; $N = 5$) (Figures 1K and 1L). In P7, P14, and adult mice, there was no difference in parenchymal intensity of CSF tracers within the hippocampus, thalamus, and striatum compared with that of cortex for all three age groups ($p > 0.05$, ANOVA).

**Figure 1. Perivascular Transport of CSF Tracers during Pre- and Post-natal Development**

(A) Drawing of an embryonic day 17.5 (E17.5) mouse embryo indicating the site of tracer injection and the different angles at which images are presented.

(B) Distribution of CSF tracers OA (45 kDa) and dextran (3 kDa) demonstrate tracer movement in caudal brain regions, midbrain and hindbrain, and along the spinal cord from injection site at cisterna magna.

(C) Images of E17.5 dissected whole brain demonstrate 45 kDa OA perivascular tracer distribution influx around the circle of Willis (white arrows) but not at the middle cerebral artery (MCA) at E17.5.

(D) Representative images of sagittal brain slices with fluorescent tracers FITC-dextran (3 kDa) and OA-Alexa Fluor 647 (OA-647) (45 kDa), 60 min after injection into the CSF of the cisterna magna in postnatal day (P) 1, P7, and P14. Scale bars, 1 mm.

(E–G) Coronal brain slices of P1 (E), P7 (F), and P14 (G). Coronal slices show some perivascular influx of 3 kDa dextran and 45 kDa OA in the cortex at P7 and more robust perivascular influx at P14. Scale bars, 1 mm.

(H–J) Higher magnification images of sagittal view of hippocampus (left) and coronal view of neocortex (right) of P1 (H), P7 (I), and P14 (J). Scale bars, 100 μm.

(K and L) Mean fluorescence intensities of (K) 3 kDa dextran and (L) 45 kDa OA-647 in hippocampus, thalamus, and striatum normalized to the mean value of cortex. The mean fluorescence intensities of 3 kDa dextran and 45 kDa OA were significantly higher in the hippocampus than cortex in P1 mice.

$^{**}p < 0.01$ and $^{***}p = 0.005$ (Student's t test), respectively. $N = 5$ for all groups. Bar graphs represent mean ± SEM.

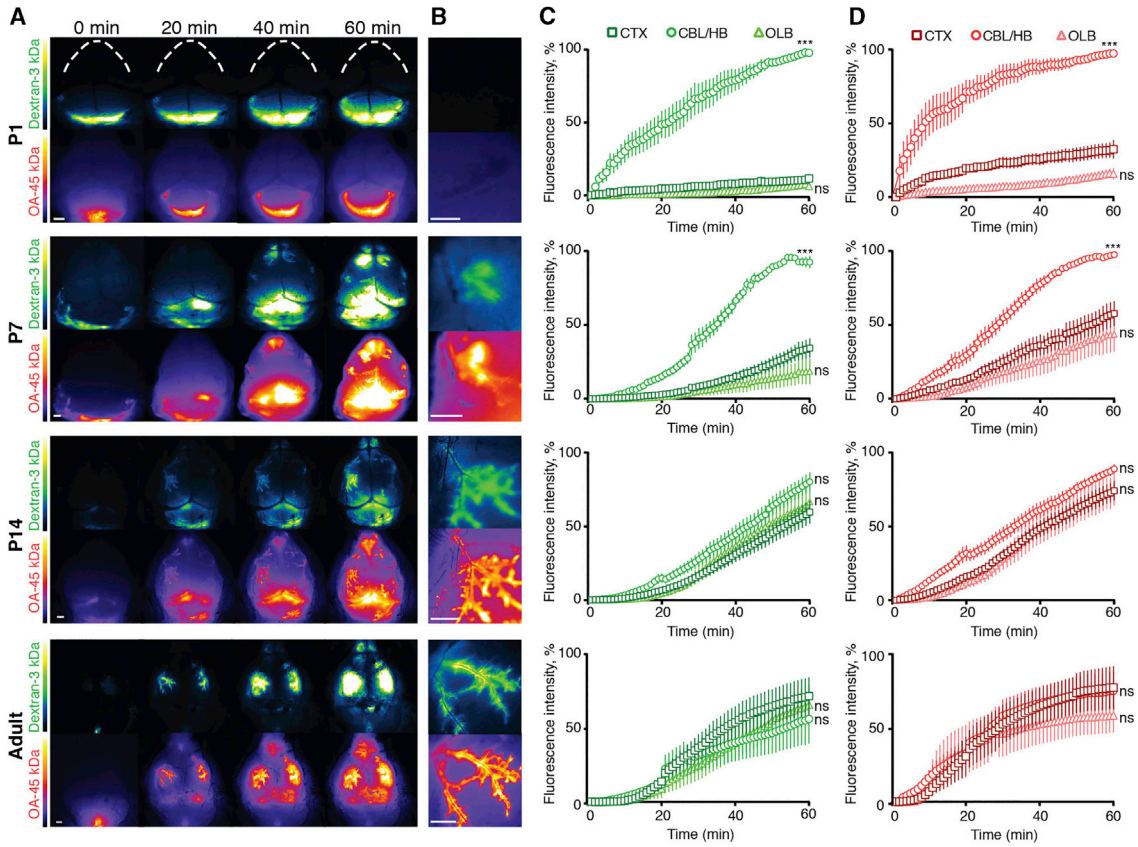


**Figure 2. *In Vivo* Time Lapse Imaging of CSF Tracers**

(A) *In vivo* images of fluorescent tracers FITC-dextran (3 kDa) and OA-Alexa 647 (45 kDa) injected into the CSF of the cisterna magna in P1, P7, P14, and adult mice at time points t = 0, 20, 40, and 60 min after injection. Scale bars, 1 mm.

(B) Higher magnification image of cortex showing perivascular tracer along the MCA in P7, P14, and adult but not at P1. Scale bars, 1 mm.

(C and D) Quantification of fluorescence signal of (C) 3 kDa dextran and (D) 45 kDa OA normalized to the highest mean intensity per area (cerebellum, cortex, or olfactory bulb) observed for each experiment.

CTX, cortex; OLB, olfactory bulb; cerebellum/hindbrain (CBL/HB) refers to hindbrain in P1 and cerebellum in P7, P14, and adult mice. In P1 mice, CSF tracers are seen slowly filling up the hindbrain compartment, while virtually no tracer reached the dorsal cortex after 60 min (N = 6). In P7 mice, perivascular influx initiated both from the olfactory bulb and slowly along middle cerebral arteries (MCAs) (N = 9). At P14 and in adult mice, the mean fluorescence intensities of both tracers were similar in all three regions of interest (N = 12 and N = 5, respectively). *$p < 0.05$, **$p < 0.01$, and ***$p < 0.001$ (two-way ANOVA); ns, non-significant. Graphs represent mean ± SEM.

## Changes in CSF Tracer Flow Patterns during Postnatal Development

To map the dynamic pattern of perivascular CSF tracer influx, in real time we injected tracers into the CSF of the cisterna magna and imaged the anesthetized mice through the intact skull (Xavier et al., 2018). In P1 mice, *in vivo* imaging showed slow tracer influx primarily into the hindbrain, while the cortex and the olfactory bulb were almost devoid of tracer influx (Figures 2A and 2B). In P7 mice, tracers were still predominantly detectable in the hind- and midbrain and cerebellum, with little influx in cortex and olfactory bulb at 60 min after tracer infusion (Figures 2C and 2D) ($p < 0.001$ for both tracers). In contrast to P1 mice, transport of tracer was observed along the perivascular spaces of the MCAs in the ventral to dorsal direction in P7 mice (Figures 2A and 2B). P14 mice differed from P7 mice in that perivascular influx along MCAs was more rapid and robust. In P14 mice, the rise in mean fluorescence intensity of CSF tracer in cortex, cerebellum, and olfactory bulb was similar throughout the course of *in vivo* imaging (Figures 2C and 2D). Transcranial macroscopic imaging of adult mice through an intact skull showed essentially the same pattern of tracer movement as the P14 mice: fast perivascular influx into the neocortex via MCAs, with mean fluorescence intensity being the same for cortex, cerebellum, and olfactory bulb (Figures 2A–2D). These observations show that although perivascular CSF pathways are present at P7, they are not fully functional. By contrast, CSF tracer distribution in P14 mice was comparable with that in adult mice, and *in vivo* imaging of perivascular influx at superficial blood vessels showed no difference in the relative distribution between cerebellum, cortex, and olfactory bulb ($p > 0.05$ for both P14–P15 and adult, two-way ANOVA) (Figures 2C and 2D).

Notably, *in vivo* imaging and brain slice imaging demonstrated that CSF tracers consistently traveled to, and intensely localized around and within, the olfactory bulb (Figures 1 and 2), which

is significant in that this region is directly coupled to the perineural and nasal lymphatic efflux routes through which CSF exits the cranial cavity (Johnston et al., 2004; Kida et al., 1993).

### Development of the Glymphatic System Is Dependent on Astrocytic Vascular Endfeet and AQP4 Polarization

In the adult brain, astrocytic AQP4 water channels are anchored specifically at the plasma membrane in the vascular endfeet, in this context called polarization of AQP4. The luminal facing surface of the vascular endfeet exhibits many fold higher AQP4 expression than the soma and perisynaptic astrocytic processes (Nagelhus et al., 1998). AQP4 water channels in astrocytic endfeet facilitate trans-membrane water flux, and genetic deletion of these channels has been shown to be associated with a 40% reduction in the efficiency of glymphatic exchange of solutes in adult mice (Iliff et al., 2012; Mestre et al., 2018). During aging, the loss of perivascular polarization of AQP4 channels correlates with reduced parenchymal CSF tracer penetration (Kress et al., 2014). To understand the mechanism responsible for targeted CSF influx to the hippocampus soon after birth, we expanded on previous developmental analyses of AQP4 by analyzing the subcellular localization of AQP4 during development (Lunde et al., 2015).

We analyzed AQP4 polarization to the vascular endfeet (Kress et al., 2014) by taking the ratio of AQP4 immunofluorescence signal at the vascular endfeet divided by the parenchymal signal in cortex and hippocampus in developing mice. At P1, AQP4 was distributed throughout the cortex in a diffuse manner and not localized to blood vessels, as in P7, P14, and adult mice (Figure 3A). At P1, AQP4 was more polarized in the stratum lacunosum and stratum moleculare regions of the hippocampus than in the cortex ($p = 0.007$) (Figures 3A–3C), correlating with the fact that perivascular tracer influx is restricted to the hippocampus in P1 mice (Figures 1E and 1H). Similarly, AQP4 polarization in the hippocampus of P7 mice was significantly higher than in the cortex ($p = 0.003$). In P14 mice, AQP4 polarization was comparable in the cortex and hippocampus. In adult mice, AQP4 polarization was higher in the cortex than in the hippocampus (Figures 3A–3C). In adult mice, AQP4 is expressed only by astrocytes, but during development radial glial cells also express AQP4 (El-Khoury et al., 2006). The majority of astrocytes developed postnatally arise from radial glial cells (Ge et al., 2012), and it is possible that radial glial cells are included in the AQP4 polarization measurements at P1 and P7.

We then used GLT1-eGFP astrocyte reporter mice (Regan et al., 2007) to evaluate the establishment of defined perivascular spaces. In the cortex of P1 pups, very few $eGFP^+$ cells were noted along the lectin-stained blood vessels. Although some $eGFP^+$ processes were in contact with the vasculature, the astrocytes were rounded and exhibited few processes and were devoid of endfeet morphology (Figure 3D). The earliest examples of a clear lining of the vasculature by GLT1-$eGFP^+$ astrocytes were found at P7 and became very prominent in P14 and adult mice, consistent with previous reports (Lunde et al., 2015; Nielsen et al., 1997).

In order to further confirm the AQP4 polarization results throughout development we measured the AQP4 content in isolated cerebral vasculature and parenchyma using western blotting. Cerebral blood vessels contain astrocytic endfeet that are tethered to the vasculature, and thus a vessel isolation approach constitutes an entirely un-biased approach (Boulay et al., 2015; Roberts et al., 2008). Measured using western blotting, the AQP4 content in the parenchymal fraction remained low throughout the different developmental ages (Figures 3E–3H and S2A–S2D). In the cortex, polarization of AQP4 to the vascular fraction was established at P14 and persisted in adulthood (Figures 3E, 3F, S2A, and S2B). Similarly, higher AQP4 content was found in the vessel isolated fraction compared with the parenchymal fraction in the hippocampus of P14 and adult mice (Figures 3G, 3H, S2C, and S2D).

Overall, glymphatic influx (Figures 1 and 2) correlated well with both the emergence of perivascular pathways, defined by astrocytic lining of the vasculature and the AQP4 content and polarization to vascular endfeet (Figure 3).

Finally, we analyzed the regional level AQP4 expression and compared with CSF tracer distribution. The highly vascularized stratum lacunosum and stratum moleculare regions of the hippocampus exhibited the highest levels of AQP4 expression at P1 (Figures 4A and 4B). The AQP4 immunofluorescence signal was also strong in the fimbriae and the part of the laterodorsal thalamic nuclei facing the ventricle, mirroring the tracer influx at P1 (Figures 4C and 4D). AQP4 immuno-intensity was highest at the pial surface of the ventral brain; lower in the thalamus, hypothalamus and piriform cortex; and negligible in the neocortex (Figure 4A).

In P7 mice the dorsal cortex of the brain reached the same level of AQP4 expression as the ventral side, but AQP4 immunofluorescence signal was higher in the hippocampus and the olfactory bulb, brain stem, and cerebellum (Figures 4E–4G). The AQP4 expression correlated with tracer influx in the hippocampus and emergence of tracer distribution to the olfactory bulb (Figures 1 and 4H–4J). In the cerebellum, AQP4 seemed to be concentrated in the white matter and in the Purkinje cell layer at P7 (Figure 4G), and this also correlated with tracer influx (Figure 4J).

In adult mice, there was a surge in AQP4 expression compared with P7 (Figure 4K), and this overall increase correlates with the more robust brain-wide perivascular influx in adult mice (Iliff et al., 2012; Kress et al., 2014; Rangroo Thrane et al., 2013; Xie et al., 2013). Exceptionally high levels of AQP4 expression were found at the olfactory bulb and in the cerebellum (Figures 4L and 4M). Consistent with closure of the recess between the cortical fold and the midbrain between P1 and P7, the tracer influx in the hippocampus was concentrated only around large arteries and was not visible on all brain slices (Figure 4N). The tracer distribution at the olfactory bulb (Figure 4O) was consistent with a high AQP4 expression and fits with the fact that the cribriform plate, via the olfactory bulb, constitute a major exit route for CSF (Bradbury and Westrop, 1983; Johnston et al., 2004). In the cerebellum, the main change in AQP4 expression from P7 to adult was the increase in expression in the molecular layer (Figures 4G and 4L), consistent with the literature (Wen et al., 1999).

In summary, the developmental profile of AQP4 expression exhibits a ventral-to-dorsal gradient, as does glymphatic tracer influx. Also, the early polarized expression of AQP4 in the hippocampus is accompanied by robust influx of CSF tracers.

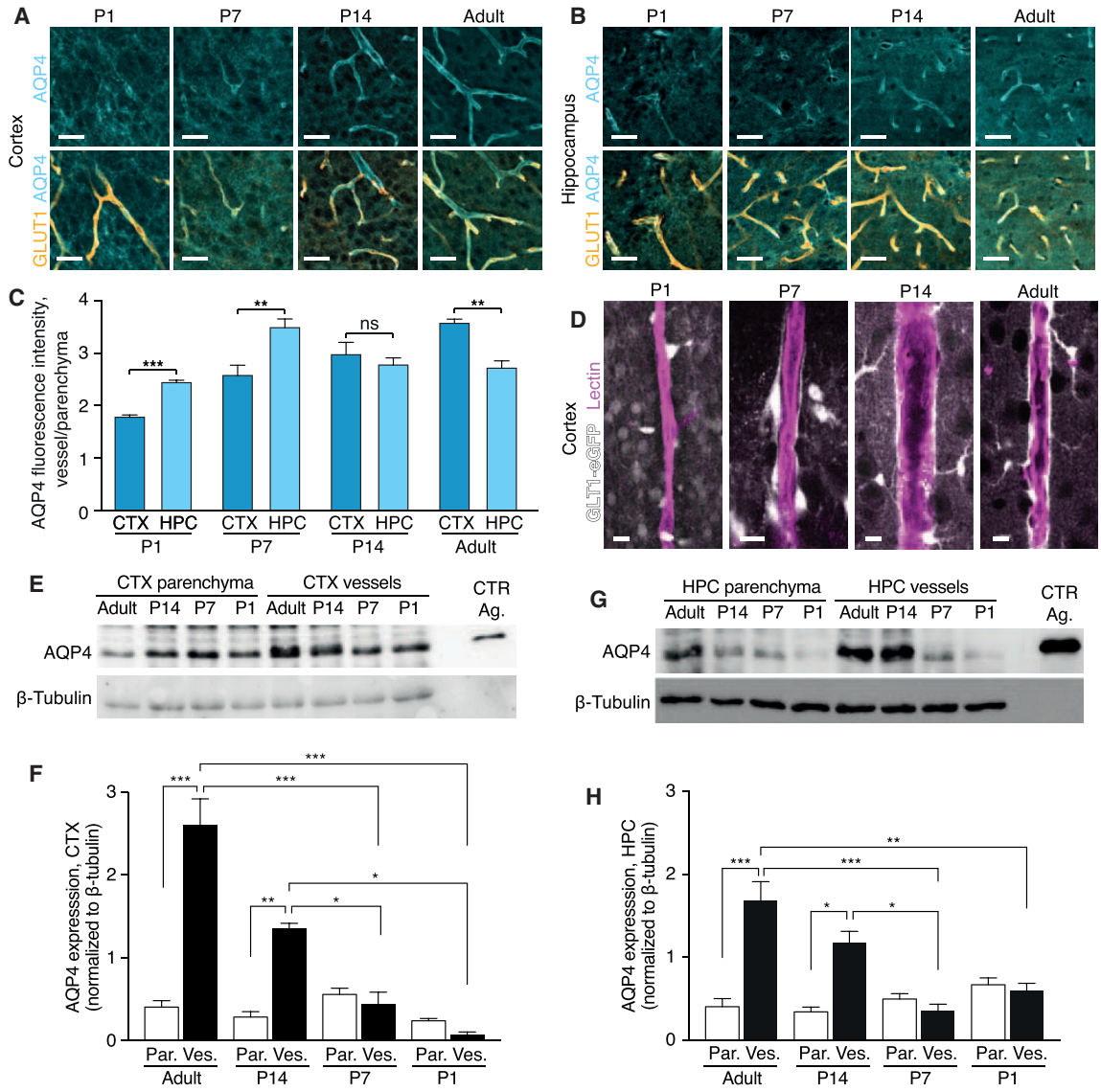


**Figure 3. AQP4 Expression and Polarization Develop Early in the Hippocampus**

(A and B) Representative confocal images of immunohistochemistry of aquaporin 4 (AQP4; cyan) and blood vessels stained for glucose transporter 1 (GLUT1; orange) at postnatal day (P) 1, P7, P14, and adult mice in (A) cortex and (B) hippocampus. Scale bars, 100 μm.

(C) Quantification of AQP4 polarization measured as the ratio of signal around the blood vessel divided by the signal in the surrounding parenchyma. Comparisons between cortex and hippocampus were performed using Student's t test. N = 4, 6, 4, and 4 for P1, P7, P14, and adult mice, respectively.

(D) Representative confocal images of lectin-labeled blood vessels and GTL1-eGFP-positive astrocytes in P1, P7, P14, and adult mouse cortex showing that astrocyte vascular endfeet development by P7. Scale bars, 10 μm.

(E–H) Representative western blot (E) and quantification (F) of AQP4 protein and β-tubulin in parenchymal and vessel isolation fraction in the cortex and (G and H) in the hippocampus. CTX, cortex; HPC, hippocampus; Par, parenchyma; Ves, vessel isolation fraction; CTR Ag, control antigen. N = 6, 5, 4, and 3 for adult, P14, P7, and P1 mice, respectively.

*p < 0.05, **p < 0.01, and ***p < 0.001 (two-way ANOVA with Tukey post-test). Bar graphs represent mean ± SEM.

## Perivascular Solute Transport Is Inhibited in PDGF-B-Deficient Mice

Pericytes emerge early in embryonic development, and several lines of work show that pericytes play a critical role in the formation and maturation of the BBB and thus the separation of the perivascular compartment from the plasma (Armulik et al., 2010; Daneman et al., 2010). Located in the perivascular space, pericytes express and secrete a number of extracellular matrix components that are known cell adhesion molecules, such as laminins and collagens (Armulik et al., 2010; Bell et al., 2010; Vanlandewijck et al., 2018). Because recruitment of pericytes to the perivascular compartment is regulated by the availability of PDGF-B signaling (Lindahl et al., 1997), we investigated perivascular transport of CSF-injected tracers in a mouse model with

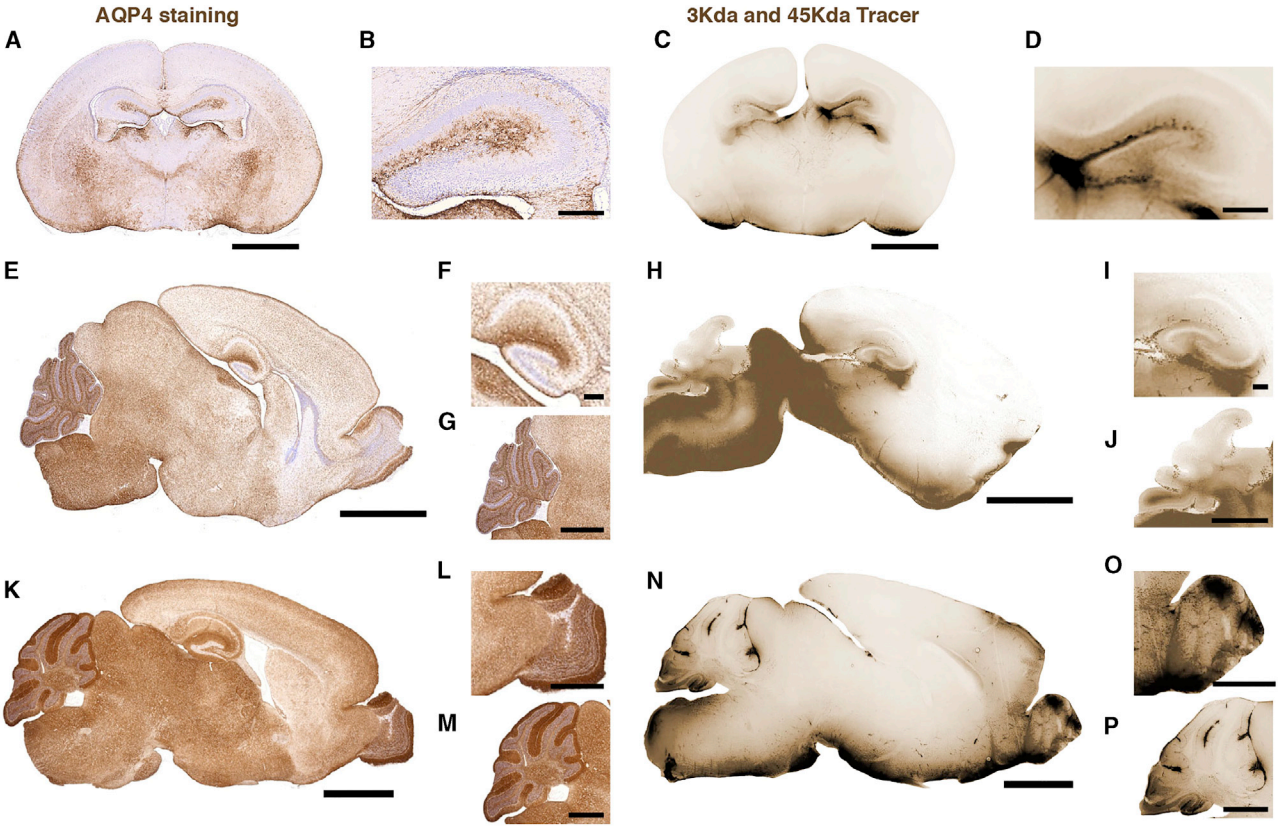


**Figure 4. AQP4 Developmental Expression Patterns Correlate with Glymphatic Influx**

Left: 4 μm brain sections stained for AQP4 (brown) and counterstained with Mayer's hematoxylin. Right: fluorescent tracers dextran (3 kDa) and OA (45 kDa) (brown) 60 min after injection into the CSF of the cisterna magna.

(A and B) AQP4 staining coronal section of P1 mouse brain. Scale bars, 1 mm (A) and 200 μm (B).

(C and D) Image of tracer influx on coronal section of P1 mouse with high magnification of hippocampus. Scale bars, 1 mm (C) and 200 μm (D).

(E–G) AQP4 staining of sagittal section of P7 mouse brain (E), hippocampus (F), and cerebellum (G). Scale bars, 2 mm, 200 μm, and 1 mm, respectively.

(H–J) Image of tracer influx on sagittal section of P7 mouse brain (H), hippocampus (I), and cerebellum (J). Scale bars, 2 mm, 200 μm, and 1 mm, respectively.

(K–M) AQP4 staining of sagittal section of adult mouse brain (K), olfactory bulb (L), and cerebellum (M). Scale bars, 2 mm, 200 μm, and 1 mm, respectively.

(N–P) Image of tracer influx on sagittal section of adult mouse brain (N), olfactory bulb (O), and cerebellum (P). Scale bars, 2 mm, 200 μm, and 1 mm, respectively.

a reduced number of pericytes, the PDGF-B retention motif knockout mice *Pdgfb*$^{ret/ret}$. PDGF-B signaling is decreased in this mouse model because of deletion of an amino acid sequence that mediates binding of PDGF-B to heparan sulfate proteoglycans and its retention in the extracellular space (Lindblom et al., 2003).

*In vivo* imaging of adult mice revealed a severely delayed or incomplete CSF tracer influx at the perivascular spaces of pial arteries of the cortex of *Pdgfb*$^{ret/ret}$ mice compared with wild-type (WT) mice (Figures 5A and 5B). Somewhat surprisingly, tracer influx was suppressed also in *Pdgfb*$^{ret/+}$ mice, although less than in *Pdgfb*$^{ret/ret}$ mice (Figures 5A and 5B). To better quantitatively assess these differences, we used threshold-defined front-tracking software to analyze the speed of peri-arterial CSF influx (Nevins and Kelley, 2017). Also, this analysis showed a significantly slower movement of CSF tracer in *Pdgfb*$^{ret/ret}$ compared with WT mice (Figures 5C and 5D).

We next assessed distribution of 45 kDa OA and 3 kDa FITC tracers in *Pdgfb*$^{ret}$ mice during postnatal development. Reduction in PDGF-B led to a decreased influx of both tracers in the hippocampus at P1 in *Pdgfb*$^{ret/+}$ (Figures 5E–5J). The main difference at P7 was a higher level of tracer influx in hippocampus in *Pdgfb*$^{ret/+}$ mice, resembling a delayed high influx in the hippocampus, which is observed in WT mice at a more immature stage (Figures 5K–5P). At P14, when cortical influx has become robust in WT mice, there was a significant decrease in influx of 45 kDa OA-Alexa Fluor 647 in the cortex (Figures 5Q–5V). Imaging of brain slices of adult *Pdgfb*$^{ret/ret}$ and *Pdgfb*$^{ret/+}$ mice confirmed the reduction in parenchymal CSF tracer penetration compared with WT mice (Figures 5W and 5X). In line with the *in vivo* imaging and front-tracking analysis (Figures 5A–5E), the mean intensity and percentage tracer penetration of CSF tracers OA-Alexa Fluor 647 (OA) (45 kDa) and FITC-dextran (3 kDa) were reduced in the cortex of adult *Pdgfb*$^{ret/ret}$ mice compared with WT mice ($p < 0.01$ for both tracers; Figures 5Y–5AB), suggesting that PDGF-B is crucial for development of the glymphatic system in the cortex in particular.

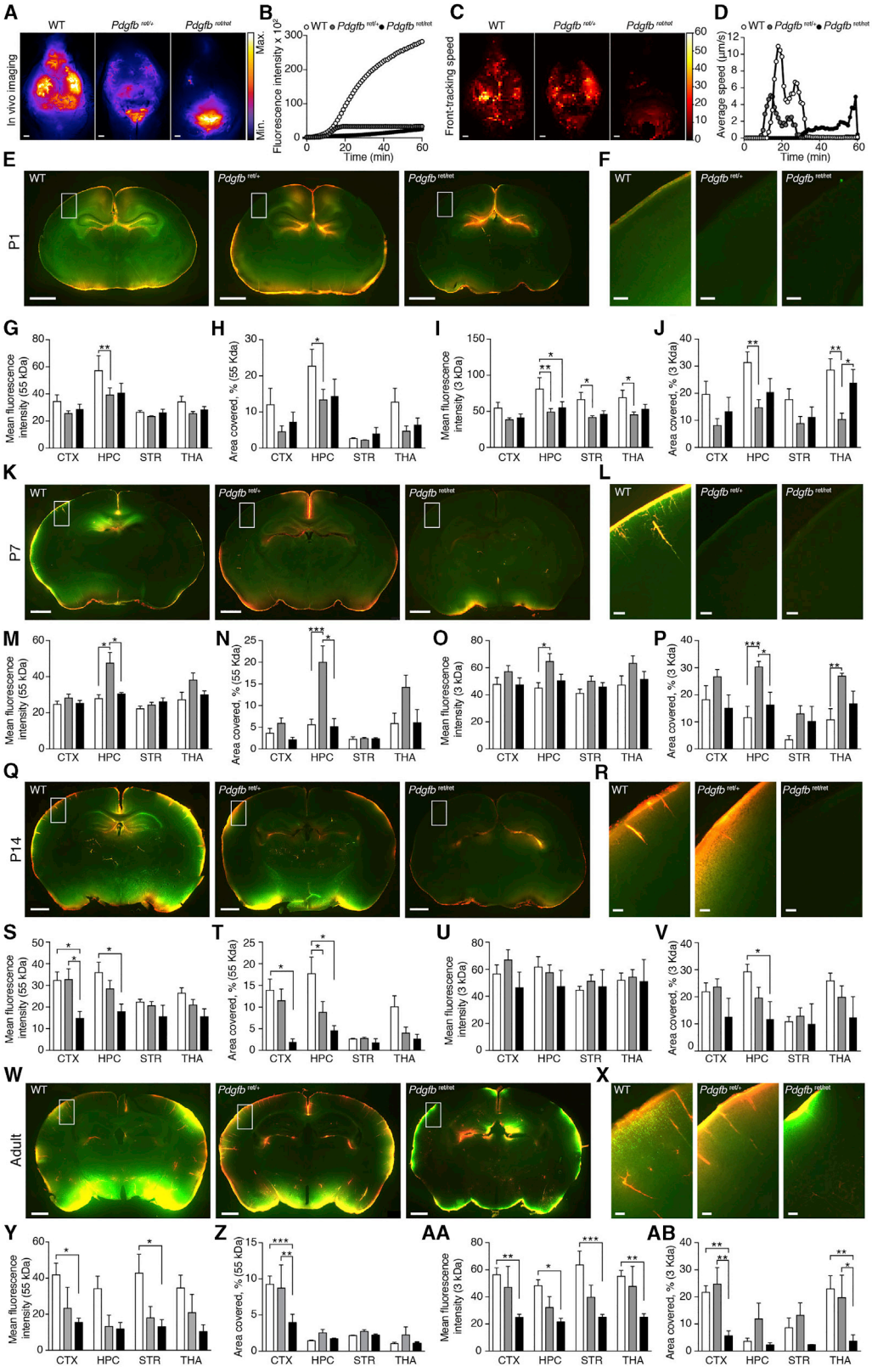


*(legend on next page)*

### Reduction of PDGF-B Signaling Causes Pericyte Deficiency and AQP4 Mislocation

PDGF-B is an essential growth factor for the development of pericytes (Lindahl et al., 1997). We therefore quantified that pericyte density in the *Pdgfb*$^{ret/+}$ and *Pdgfb*$^{ret/ret}$ mice. Consistent with previous reports for pericyte coverage of cerebral blood vessels in these mice (Armulik et al., 2010), pericyte density was reduced by 91.5% ± 2.0% in the cortex of adult *Pdgfb*$^{ret/ret}$ mice ($p < 0.0001$) (Figures 6A and 6B). Our analysis revealed a 66.0% ± 6.8% reduction of pericyte density in the *Pdgfb*$^{ret/+}$ mice ($p < 0.0001$) (Figures 6A and 6B). These data show functional abnormalities in *Pdgfb*$^{ret/+}$ mice, indicating that two WT copies are needed for optimal function of PDGF-B and pericyte recruitment. Interestingly, in the *Pdgfb*$^{ret/ret}$ mice, but not in the *Pdgfb*$^{ret/+}$ mice, 62.5% ± 13.9% ($p = 0.0006$) of the pericytes' cell bodies lacked a close spatial relationship with AQP4-positive blood vessel branches, but often extended processes that wrapped around AQP4-positive blood vessels (Figure 6C). The mean intensity of AQP4 staining in the *Pdgfb*$^{ret/+}$ and *Pdgfb*$^{ret/ret}$ mice was found to be reduced by 42.5% ± 4.5% ($p = 0.0001$) and 36.5% ± 4.9% ($p = 0.0064$) in the cortex, respectively (Figure 6D). Similar reduction in pericyte density, pericytes' association with blood vessels, and overall AQP4 immunofluorescent signal were found in the hippocampus of *Pdgfb*$^{ret/+}$ and *Pdgfb*$^{ret/ret}$ mice (Figures 6E–6H).

Pericytes express laminin α2 and agrin (Vanlandewijck et al., 2018), both of which bind to α-dystroglycan, which connects to α-syntrophin and dystrophin as part of an anchoring complex (dystrophin-associated protein complex [DAPC]) for AQP4 in the astrocyte endfeet (Neely et al., 2001; Wolburg et al., 2011). We therefore investigated the polarization of AQP4 in the *Pdgfb*$^{ret}$ mouse strain. In the cortex of *Pdgfb*$^{ret/+}$ and *Pdgfb*$^{ret/ret}$ mice, AQP4 polarization toward the vasculature and away from parenchymal processes (polarization index) was reduced by 18.3% ± 2.8% and 37.6% ± 3.5%, respectively ($p < 0.0001$ for both genotypes). Polarization in the hippocampus was reduced by 17.4% ± 3.7% and 33.8% ± 3.3%, respectively ($p < 0.0001$ for *Pdgfb*$^{ret/ret}$, $p < 0.01$ for *Pdgfb*$^{ret/+}$) (Figures 6I–6N). The redistribution of AQP4 from the astrocyte endfeet to the cell bodies in adult *Pdgfb*$^{ret/ret}$ mice thus mimicked what distribution pattern we observed for early postnatal ages.

In order to complement the immunohistochemical analysis of perivascular AQP4, we assessed AQP4 protein expression in cerebral vessel isolations and parenchyma separated from the same brain homogenates using western blotting. The results revealed no difference in parenchymal AQP4 content per mg protein in the heterozygous or homozygous *Pdgfb*$^{ret}$ mice compared with WT mice (Figures 6O–6Q, S3A, and S3B). However, in both cortex and hippocampus, there was significantly higher AQP4 protein expression in the vascular fraction compared with the parenchymal fraction in both the WT and the *Pdgfb*$^{ret/wt}$ mice but not in the *Pdgfb*$^{ret/ret}$ mice, indicating that polarization of AQP4 to the vascular endfeet was perturbed in when PDGF-B signaling is reduced (Figures 6O–6Q).

Thus, using two independent methods, our results showed that AQP4 polarization to the vasculature depends on the availability of PDGF-B, both for the cortex and for the hippocampus.

## DISCUSSION

Fluid transport in perivascular pathways has been implicated in clearance of solutes and proteins from the brain (Iliff et al., 2012; Lundgaard et al., 2017; Mestre et al., 2018; Xie et al., 2013) but has been sparsely studied in development (Di Palma et al., 2018). A recent MRI study demonstrated that the glymphatic system is developed by P90, although statistical significance was not indicated between P28 and P90 (Di Palma et al., 2018). Because of the resolution limitations of MRI, our study adds a characterization of perivascular CSF influx in early postnatal ages. We show that perivascular solute transport displays initial signs of development at the arterial circle of Willis at E17.5, starts in the hippocampal parenchyma in newborn mice, and then develops in a ventral-to-dorsal manner, reaching the superficial dorsal cortex in P7 mice, and becomes mature by P14 (Figure 7A). Our data confirm that perivascular CSF influx depends AQP4 expression, particularly AQP4 polarization to the astrocytic endfeet in the developing brain (Figure 7B). We measured AQP4 polarization both using immunohistochemistry and by comparing protein analysis in cerebral vessel isolation and parenchymal fractions. Both methods were able to detect robust polarization of AQP4 at P14 and in adult mice, whereas only immunohistochemistry was able to detect polarization in P1 and P7 mice. Remarkably, we found that the glymphatic system is strikingly sensitive to the amount and localization of PDGF-B signaling.

In this study, we used two tracers, FITC-dextran (3 kDa) and OA-Alexa 647 (45 kDa), which are both negatively charged but of different molecular weights. Studies have shown that both hydrophobic and hydrophilic tracers are transported in the perivascular space (Rangroo Thrane et al., 2013), but the importance of molecular shape and positive versus negative charge remains to be explored. It cannot be ruled out that the degree of tracer penetration is affected by molecular shape and charge more so than the molecular weight.

**Figure 5. PDGF-B Signaling Is Needed for Development of the Glymphatic System**

(A and B) Representative *in vivo* images at 60 min (A) and quantification (B) of CSF tracer ovalbumin (OA)-Alexa 647 (OA-647) (45 kDa) injected in the cisterna magna of adult in wild-type (WT), Pdgfb$^{ret/+}$, and Pdgfb$^{ret/ret}$ mice. Scale bars, 1 mm.

(C and D) Cumulative speed map (C) and quantification (D) of average influx speedusing front-tracking analysis of OA-647 tracer in adult WT, Pdgfb$^{ret/+}$, and Pdgfb$^{ret/ret}$ mice.

(E, K, Q and W)Representative images of CSF tracers OA-647 (45 kDa; red) and FITC-dextran (3 kDa; green) of whole brain and (F, L, R, and X) insets of cortex. (G, M, S, and Y) quantification of mean fluorescence intensity of OA-647 and (H, N, T, and Z) percentage area covered by tracer.

(I, O, U, and AA) Quantification of mean fluorescence intensity of FITC-dextran and (J, P, V, and AB) percentage area covered by tracer.

CTX, cortex; HPC, hippocampus; STR, striatum; THA, thalamus. In (E)–(AB), N for WT, Pdgfb$^{ret/+}$, and Pdgfb$^{ret/ret}$ = 7, 17, and 7 for P1; 6, 12, and 4 for P7; 15, 15, and 4 for P14; and 5, 4, and 5 for adult, respectively. Scale bars, 1 mm. *$p < 0.05$, **$p < 0.01$, and ***$p < 0.001$ (two-way ANOVA with Tukey test). Bar graphs represent mean ± SEM.

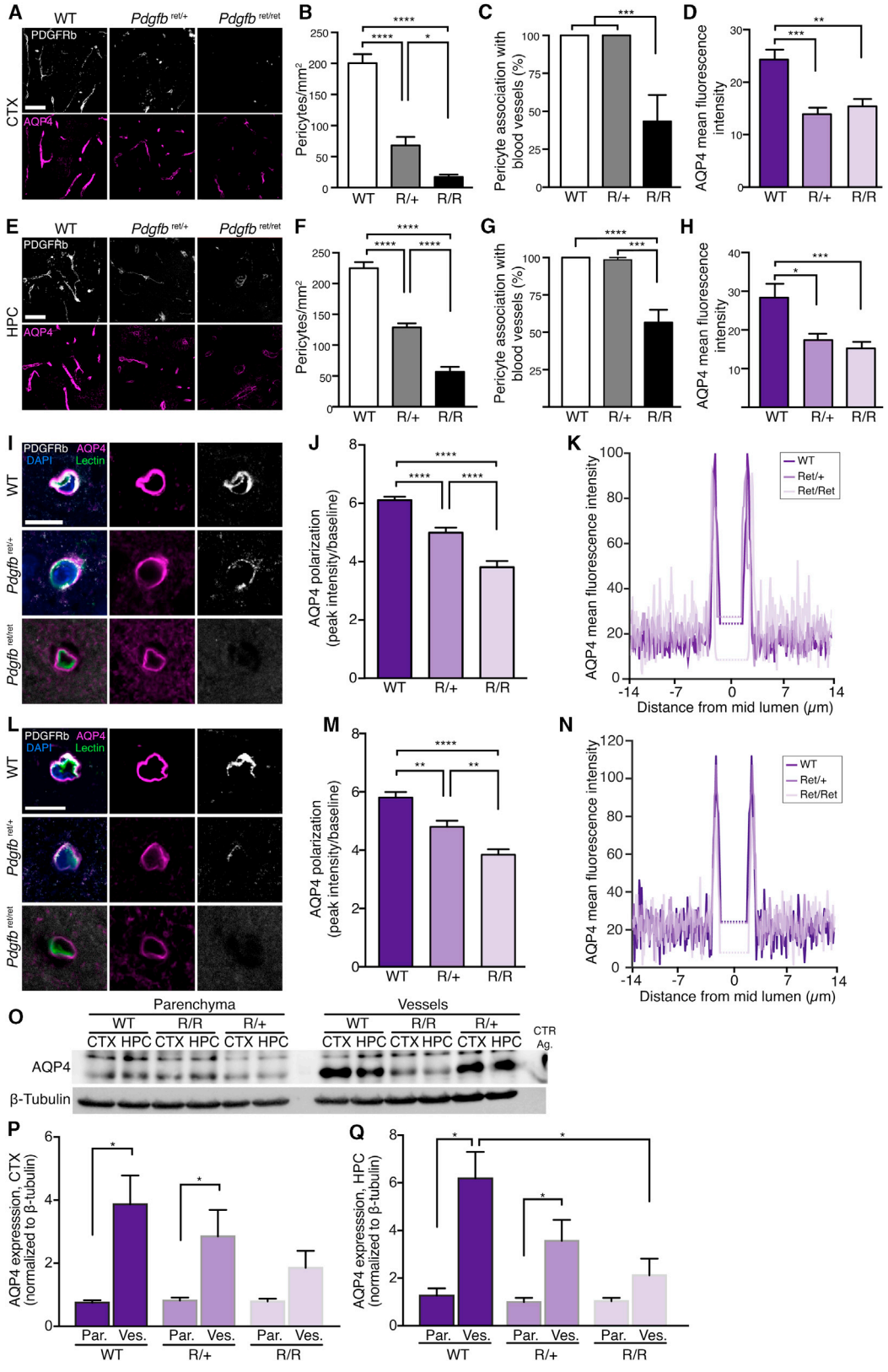


*(legend on next page)*

Our results show that perivascular solute transport emerges surprisingly late in development compared with maturation of the individual cell types (Figure 7C). For CSF to be transported from the subarachnoid space into perivascular pathways, CSF must be produced by the choroid plexus, the BBB formed, and astrocytic endfeet containing AQP4 channels developed, prior to establishment of glymphatic transport. Choroid plexus epithelium exists as early as embryonic day 14 (E14) (Sturrock, 1979), and already at E15, key solute carriers are expressed by the choroid plexus epithelial cells (Saunders et al., 2012), suggesting that CSF production starts at this time in embryonic development. Exclusion of large blood-borne tracers has been observed as early as E15.5 and indicates that the BBB also is developed around the same time, although trans-endothelial resistance in subarachnoid blood vessels is far below adult levels until E21 (Ben-Zvi et al., 2014; Butt et al., 1990; Daneman et al., 2010; Saunders et al., 2012, 2016), and barrier functions change with time until adulthood (Whish et al., 2015). Pericytes appear in synchrony with endothelial cells and migrate to newly formed capillaries orchestrated by PDGF-B signaling by endothelial cells (Lindahl et al., 1997). Pericytes may play an important role in stabilization of the BBB formed by the endothelial cells (Daneman et al., 2010) and thus in models in which PDGF-B signaling is compromised could potentially be confounded by a potential disruption of the BBB. Astrocytes are generated at a modest tempo starting at ~E18 in mice and grow more rapidly in number postnatally until the second postnatal week (Ge et al., 2012), by which time astrocytic endfeet ensheath the vasculature efficiently and AQP4 is concentrated at the endfeet. Our results thus confirm and extend the notion that astrocytes and endfoot polarization of AQP4 is crucial for perivascular solute transport (Iliff et al., 2012; Mestre et al., 2018), even during development.

The meningeal lymphatic system develops in a similar pattern as the glymphatic system, starting at foramen magnum at the base of the skull around P0, reaching halfway up the middle meningeal artery, a meningeal artery following an anatomically similar pathway to the MCA, along the lateral aspect of the brain, by P8 (Antila et al., 2017). The last part of the meningeal lymphatics to develop are located in proximity to the superior sagittal sinus, developing in the most posterior parts by P20, 1 week after the glymphatic system is fully developed in the dorsal cortex (Antila et al., 2017). The close temporal and spatial association between the glymphatic system and the meningeal lymphatic system suggests that glymphatic clearance and the meningeal lymphatic system are part of the same pathway for effective removal of solutes from the brain (Aspelund et al., 2015; Louveau et al., 2015), in addition to the route via the cribriform plate (Bradbury and Westrop, 1983; Johnston et al., 2004; Kida et al., 1993; Mollanji et al., 2002; Silver et al., 2002).

Interestingly, the first brain region to receive robust influx of CSF tracers was the hippocampus. The highest rate of postnatal hippocampal neurogenesis occurs between P0 and P7, when the glymphatic system is predominantly reaching the hippocampus, and this coincides with a peak in the protein content in CSF that occurs at P0 (Dziegielewska et al., 1981). The major source of thyroxine in the brain is transported from the blood to the CNS across the choroid plexus (Dickson et al., 1987), and the hippocampus is particularly vulnerable to postnatal lack of thyroid hormone (Madeira et al., 1992). Combining these facts with the finding that CSF transport is targeted to the hippocampus in early postnatal development suggests a role for the glymphatic system in delivery of thyroxine and possible other critical factors to the hippocampus in early postnatal development.

Knockout of the *Pdgfb* gene is embryonically lethal (Levéen et al., 1994), but the viable *Pdgfb*$^{ret/ret}$ mouse line carrying a deletion of the PDGF-B retention domain made it possible to study the consequences of impaired PDGF-B signaling for postnatal glymphatic development. PDGF-B signals via PDGF receptor-beta, which is expressed by brain pericytes at all stages of development (Jung et al., 2018), and this signaling is crucial for recruitment of pericytes to the brain vasculature (Hellström et al., 1999; Lindahl et al., 1997). *Pdgfb*$^{ret/ret}$ mice, which despite a large reduction in pericyte density (Lindblom et al., 2003) survive into adulthood, permit the analysis of the consequences of pericyte loss for brain function. Prior to the discovery of the glymphatic system, it was noted that aberrant pericyte expression resulted in abnormal AQP4 expression around cortical blood vessels (Armulik et al., 2010). Using immunohistochemistry and western blot of vessel isolations, we confirmed the reduced polarization of AQP4 to vascular endfeet. In addition, we found that *Pdgfb*$^{ret/ret}$ mice fail to develop proper glymphatic function, first detectable in the hippocampus at P1 and in the cortex at

**Figure 6. AQP4 Endfeet Polarization Is Dependent on the Presence of Pericytes**

(A and E) Representative images of PDGFRb (pericytes; white) and AQP4 (magenta) immunostaining in cortex (A) and hippocampus (E). Scale bars, 50 μm.

(B and F) Quantification of pericyte density in cortex (B) and hippocampus (F) (n = 12, all groups).

(C and G) Percentage of pericyte cell bodies localized perivascularly in cortex (C) (n = 12, 12, and 8 for control, *Pdgfb*$^{ret/+}$, and *Pdgfb*$^{ret/ret}$, respectively) and hippocampus (G) (n = 12, 12, and 11 for control, *Pdgfb*$^{ret/+}$, and *Pdgfb*$^{ret/ret}$, respectively).

(D and H) Mean AQP4 intensity in cortex (D) and hippocampus (H) (n = 12, all groups).

(I and L) Representative images of AQP4 (magenta), PDGFRb (white), *Lycopersicon esculentum* lectin (green), and DAPI (blue) of WT, *Pdgfb*$^{ret/+}$, and *Pdgfb*$^{ret/ret}$ in cortex (I) and hippocampus (L). Scale bar, 10 μm.

(J and M) AQP4 polarization and (K and N) model of fluorescence intensity plot for mean baseline, variance, peak and intraluminal intensity (dotted line) in the cortex and hippocampus (n = 15, 12, and 12 for control, *Pdgfb*$^{ret/+}$, and *Pdgfb*$^{ret/ret}$, respectively).

(O) Representative western blot of AQP4 and β-tubulin parenchyma and vessel isolation fraction of WT, *Pdgfb*$^{ret/+}$, and *Pdgfb*$^{ret/ret}$ mice. WT, wild-type; R/R, *Pdgfb*$^{ret/ret}$; R/+, *Pdgfb*$^{ret/+}$; CTR ag, AQP4 control antigen.

(P and Q) Quantification of AQP4 western blot in parenchyma (par.) and vessel fraction (ves.) in cortex (P) and hippocampus (Q). N = 6, 7, and 6 for WT, *Pdgfb*$^{ret/+}$, and *Pdgfb*$^{ret/ret}$, respectively.

In (C), (D), (G), and (H), one-way ANOVA with Tukey test for multiple comparisons for normally distributed data. In (B), (F), (J), and (M), Kruskal-Wallis with Dunn's test for data not distributed normally. In (P) and (Q), two-way ANOVA with Dunnett test. *$p < 0.05$, **$p < 0.01$, ***$p < 0.001$, and ****$p < 0.0001$. Bar graphs represent mean ± SEM.

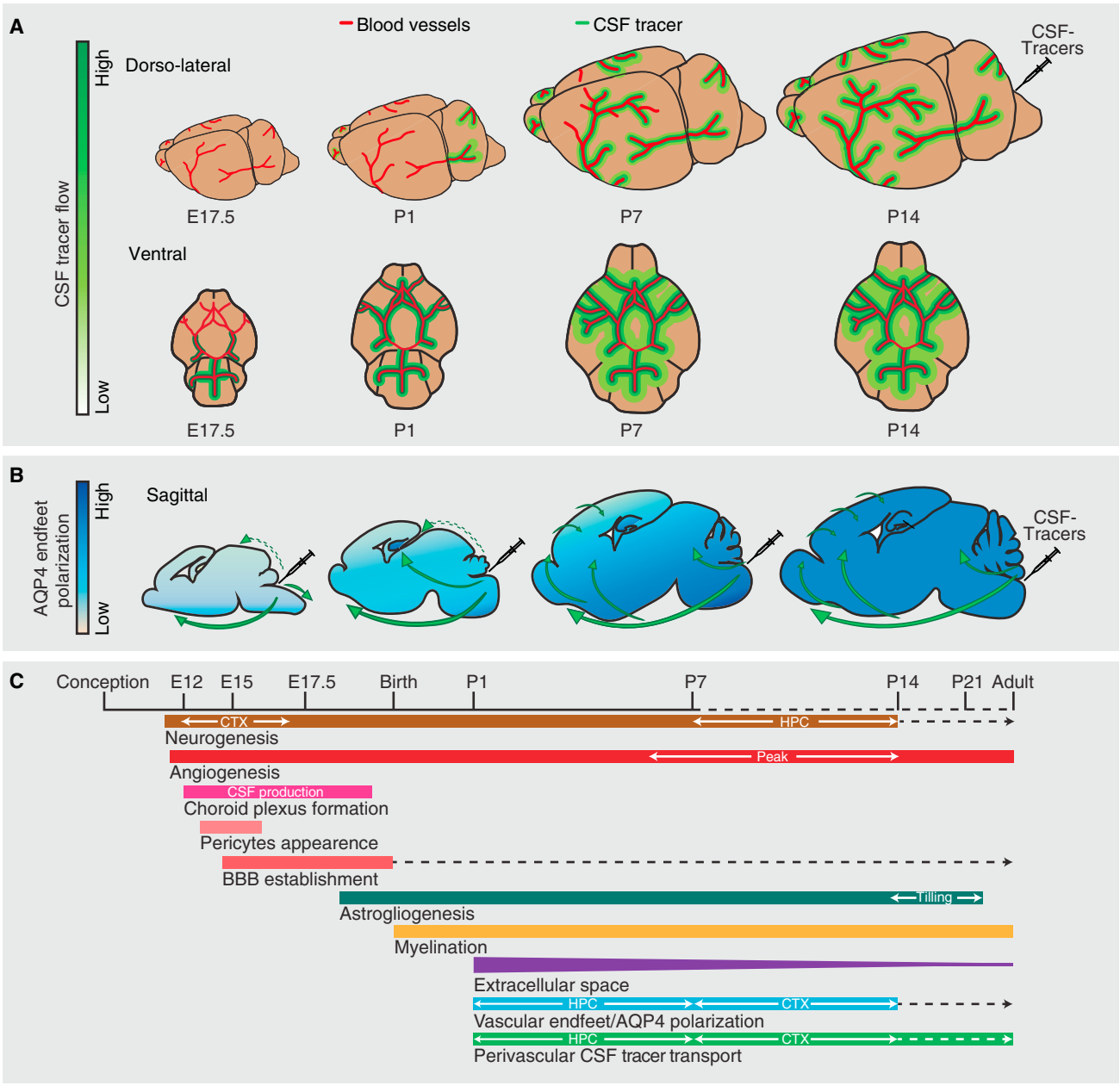


**Figure 7. Glymphatic Flow Patterns during Development and Concurrent Developmental Events**

(A) Dorso-lateral view depicts the distribution patterns of CSF tracers in perivascular pathways of the MCA at mouse E17.5 and postnatal day (P) 1, P7, and P14. Ventral view shows the arterial circle of Willis and beginning of MCAs. Ventral perivascular flow along the circle of Willis is very faint at E17.5 and fully developed at P1. At P1 tracer is seen along the proximal part of the MCAs, and from P8 CSF tracer reaches dorsal cortex via the MCA perivascular space. Cortical glymphatic influx occurs starting at P7 and increases during brain maturation.

(B) Aquaporin 4 (AQP4) polarization to astrocytes' vascular endfeet increases with age. AQP4 polarization is more pronounced in the hippocampus than in the cortex at P1 and P7. Direction of CSF influx illustrated on the sagittal drawings; dashed green arrows show compartment flow entering hippocampus, possibly due to structural opening in P1 mice and further facilitated into the hippocampal parenchyma by AQP4 in the stratum radiatum and stratum moleculare. Solid green arrows visualize the glymphatic flow of CSF tracers facilitated by perivascular AQP4 water channels.

(C) Timeline represents some key developmental events in the mouse brain, with temporal orchestration shown in relation to the establishment of the glymphatic system (perivascular CSF tracer transport). Dashed lines indicate continued development at a reduced tempo, opposite to solid lines indicating an increase. CSF, cerebrospinal fluid; BBB, blood-brain barrier; HPC, hippocampus; CTX, cortex.

P14, the latter persisting into adulthood. This indicates that pericytes, a cell type in the CNS relying heavily on PDGF-B signaling (Lindahl et al., 1997), might play a major role in the development of the glymphatic system, though it cannot be ruled out that the effects are mediated by vascular smooth muscle cells expressing PDGF receptor-beta (PDGFRb) (Hellström et al., 1999) or fibroblast-like perivascular cells via PDGF-B signaling to PDGF receptor-alpha (PDGFRα) (Boström et al., 2002; Vanlandewijck et al., 2018) or disruption of the BBB (Daneman et al., 2010).

PDGF-B is thus a growth factor associated with development of glymphatic function. Future studies detailing the molecular interactions between pericytes and astrocytes are important for understanding the development of the glymphatic system and will likely also provide insight into why glymphatic flow declines in aging and why so many neurological diseases negatively affect glymphatic function (Achariyar et al., 2016; Gaberel et al., 2014; Goulay et al., 2017; Iliff et al., 2014; Jiang et al., 2017; Kress et al., 2014; Peng et al., 2016; Schain et al., 2017; Wang et al., 2017).

## STAR★METHODS

Detailed methods are provided in the online version of this paper and include the following:

- KEY RESOURCES TABLE
- CONTACT FOR REAGENT AND RESOURCE SHARING
- EXPERIMENTAL MODEL & SUBJECT DETAILS
- METHOD DETAILS
  - Anesthesia
  - Intracisternal tracer infusion procedure
  - Embryonic tracer infusion and imaging
  - *In vivo* tracer influx imaging
  - Immunohistochemisty and lectin labeling
  - Isolation of cerebral blood vessels
  - Western blotting
- QUANTIFICATION AND STATISTICAL ANALYSES
  - AQP4 polarization analysis
  - *In vivo* tracer influx quantification
  - Western blotting
  - Tracer influx tracking
  - Statistics

### SUPPLEMENTAL INFORMATION

Supplemental Information can be found with this article online at https://doi.org/10.1016/j.celrep.2019.02.050.

### ACKNOWLEDGMENTS

This work was funded by the NIH/NINDS RO1 AG057575-01, the NIH/NIA, the Novo Nordisk Foundation, the Lundbeck Foundation, the Adelson Medical Research Foundation, the European Union (EU) Joint Programme – Neurodegenerative Disease Research (JPND) program, the EU Horizon 2020 Research and Innovation Program grant agreement 643417/DACAPO-AD, the Swedish Science Council VR 2015-00550, the Swedish Cancer Foundation CF 15 0735, and the Knut & Alice Wallenberg Foundation 2015.0030 and starting grant. We thank Wei Song, Ezra Yang, and Allison Eberhardt for technical assistance. Lund University Bioimaging Center (LBIC) is gratefully acknowledged for providing access to Nikon confocal microscope system A1+. Finally, we are grateful for the time we were able to spend with our dear friend and colleague Benjamin T. Kress, who was immensely talented for science and passed away much too young.

### AUTHOR CONTRIBUTIONS

A.S.M., W.W., N.B.B., A.M.E., A.X.C., B.S., A.B., M.A.M., B.T.K., D.H.K., K.M., A.M., and I.L. performed experiments and analyzed data. A.S.M., C.B., K.M., M.N., and I.L. wrote the manuscript. C.B., K.M., A.M., M.N., and I.L. contributed reagents.

### DECLARATION OF INTERESTS

The authors declare no competing interests.

Received: July 3, 2018
Revised: January 7, 2019
Accepted: February 13, 2019
Published: March 12, 2019

### REFERENCES

Achariyar, T.M., Li, B., Peng, W., Verghese, P.B., Shi, Y., McConnell, E., Benraiss, A., Kasper, T., Song, W., Takano, T., et al. (2016). Glymphatic distribution of CSF-derived apoE into brain is isoform specific and suppressed during sleep deprivation. Mol. Neurodegener. *11*, 74.

Antila, S., Karaman, S., Nurmi, H., Airavaara, M., Voutilainen, M.H., Mathivet, T., Chilov, D., Li, Z., Koppinen, T., Park, J.H., et al. (2017). Development and plasticity of meningeal lymphatic vessels. J. Exp. Med. *214*, 3645–3667.

Armulik, A., Genové, G., Mäe, M., Nisancioglu, M.H., Wallgard, E., Niaudet, C., He, L., Norlin, J., Lindblom, P., Strittmatter, K., et al. (2010). Pericytes regulate the blood-brain barrier. Nature *468*, 557–561.

Aspelund, A., Antila, S., Proulx, S.T., Karlsen, T.V., Karaman, S., Detmar, M., Wiig, H., and Alitalo, K. (2015). A dural lymphatic vascular system that drains brain interstitial fluid and macromolecules. J. Exp. Med. *212*, 991–999.

Balslev, Y., Saunders, N.R., and Møllgård, K. (1997). Ontogenetic development of diffusional restriction to protein at the pial surface of the rat brain: an electron microscopical study. J. Neurocytol. *26*, 133–148.

Bell, R.D., Winkler, E.A., Sagare, A.P., Singh, I., LaRue, B., Deane, R., and Zlokovic, B.V. (2010). Pericytes control key neurovascular functions and neuronal phenotype in the adult brain and during brain aging. Neuron *68*, 409–427.

Ben-Zvi, A., Lacoste, B., Kur, E., Andreone, B.J., Mayshar, Y., Yan, H., and Gu, C. (2014). Mfsd2a is critical for the formation and function of the blood-brain barrier. Nature *509*, 507–511.

Boström, H., Gritli-Linde, A., and Betsholtz, C. (2002). PDGF-A/PDGF alpha-receptor signaling is required for lung growth and the formation of alveoli but not for early lung branching morphogenesis. Dev. Dyn. *223*, 155–162.

Boulay, A.C., Saubaméa, B., Declèves, X., and Cohen-Salmon, M. (2015). Purification of mouse brain vessels. J. Vis. Exp. (*105*), e53208.

Bradbury, M.W., and Westrop, R.J. (1983). Factors influencing exit of substances from cerebrospinal fluid into deep cervical lymph of the rabbit. J. Physiol. *339*, 519–534.

Butt, A.M., Jones, H.C., and Abbott, N.J. (1990). Electrical resistance across the blood-brain barrier in anaesthetized rats: a developmental study. J. Physiol. *429*, 47–62.

Daneman, R., Zhou, L., Kebede, A.A., and Barres, B.A. (2010). Pericytes are required for blood-brain barrier integrity during embryogenesis. Nature *468*, 562–566.

Di Palma, C., Goulay, R., Chagnot, S., Martinez De Lizarrondo, S., Anfray, A., Salaun, J.P., Maubert, E., Lechapt-Zalcman, E., Andreiuolo, F., Gakuba, C., et al. (2018). Cerebrospinal fluid flow increases from newborn to adult stages. Dev. Neurobiol. *78*, 851–858.

Dickson, P.W., Aldred, A.R., Menting, J.G., Marley, P.D., Sawyer, W.H., and Schreiber, G. (1987). Thyroxine transport in choroid plexus. J. Biol. Chem. *262*, 13907–13915.

Dorr, A., Sled, J.G., and Kabani, N. (2007). Three-dimensional cerebral vasculature of the CBA mouse brain: a magnetic resonance imaging and micro computed tomography study. Neuroimage *35*, 1409–1423.

Dziegielewska, K.M., Evans, C.A., Lai, P.C., Lorscheider, F.L., Malinowska, D.H., Møllgård, K., and Saunders, N.R. (1981). Proteins in cerebrospinal fluid and plasma of fetal rats during development. Dev. Biol. *83*, 193–200.

El-Khoury, N., Braun, A., Hu, F., Pandey, M., Nedergaard, M., Lagamma, E.F., and Ballabh, P. (2006). Astrocyte end-feet in germinal matrix, cerebral cortex, and white matter in developing infants. Pediatr. Res. *59*, 673–679.

Gaberel, T., Gakuba, C., Goulay, R., Martinez De Lizarrondo, S., Hanouz, J.L., Emery, E., Touze, E., Vivien, D., and Gauberti, M. (2014). Impaired glymphatic perfusion after strokes revealed by contrast-enhanced MRI: a new target for fibrinolysis? Stroke *45*, 3092–3096.

Ge, W.P., Miyawaki, A., Gage, F.H., Jan, Y.N., and Jan, L.Y. (2012). Local generation of glia is a major astrocyte source in postnatal cortex. Nature *484*, 376–380.

Goulay, R., Flament, J., Gauberti, M., Naveau, M., Pasquet, N., Gakuba, C., Emery, E., Hantraye, P., Vivien, D., Aron-Badin, R., and Gaberel, T. (2017). Subarachnoid hemorrhage severely impairs brain parenchymal cerebrospinal fluid circulation in nonhuman primate. Stroke *48*, 2301–2305.

Hellström, M., Kalén, M., Lindahl, P., Abramsson, A., and Betsholtz, C. (1999). Role of PDGF-B and PDGFR-beta in recruitment of vascular smooth muscle cells and pericytes during embryonic blood vessel formation in the mouse. Development *126*, 3047–3055.

Iliff, J.J., Wang, M., Liao, Y., Plogg, B.A., Peng, W., Gundersen, G.A., Benveniste, H., Vates, G.E., Deane, R., Goldman, S.A., et al. (2012). A paravascular pathway facilitates CSF flow through the brain parenchyma and the clearance of interstitial solutes, including amyloid β. Sci. Transl. Med. *4*, 147ra111.

Iliff, J.J., Chen, M.J., Plog, B.A., Zeppenfeld, D.M., Soltero, M., Yang, L., Singh, I., Deane, R., and Nedergaard, M. (2014). Impairment of glymphatic pathway function promotes tau pathology after traumatic brain injury. J. Neurosci. *34*, 16180–16193.

Jiang, Q., Zhang, L., Ding, G., Davoodi-Bojd, E., Li, Q., Li, L., Sadry, N., Nedergaard, M., Chopp, M., and Zhang, Z. (2017). Impairment of the glymphatic system after diabetes. J. Cereb. Blood Flow Metab. *37*, 1326–1337.

Johnston, M., Zakharov, A., Papaiconomou, C., Salmasi, G., and Armstrong, D. (2004). Evidence of connections between cerebrospinal fluid and nasal lymphatic vessels in humans, non-human primates and other mammalian species. Cerebrospinal Fluid Res. *1*, 2.

Jung, B., Arnold, T.D., Raschperger, E., Gaengel, K., and Betsholtz, C. (2018). Visualization of vascular mural cells in developing brain using genetically labeled transgenic reporter mice. J. Cereb. Blood Flow Metab. *38*, 456–468.

Kida, S., Pantazis, A., and Weller, R.O. (1993). CSF drains directly from the subarachnoid space into nasal lymphatics in the rat. Anatomy, histology and immunological significance. Neuropathol. Appl. Neurobiol. *19*, 480–488.

Korogod, N., Petersen, C.C., and Knott, G.W. (2015). Ultrastructural analysis of adult mouse neocortex comparing aldehyde perfusion with cryo fixation. eLife *4*.

Kress, B.T., Iliff, J.J., Xia, M., Wang, M., Wei, H.S., Zeppenfeld, D., Xie, L., Kang, H., Xu, Q., Liew, J.A., et al. (2014). Impairment of paravascular clearance pathways in the aging brain. Ann. Neurol. *76*, 845–861.

Lehmenkühler, A., Syková, E., Svoboda, J., Zilles, K., and Nicholson, C. (1993). Extracellular space parameters in the rat neocortex and subcortical white matter during postnatal development determined by diffusion analysis. Neuroscience *55*, 339–351.

Levéen, P., Pekny, M., Gebre-Medhin, S., Swolin, B., Larsson, E., and Betsholtz, C. (1994). Mice deficient for PDGF B show renal, cardiovascular, and hematological abnormalities. Genes Dev. *8*, 1875–1887.

Liddelow, S.A., Dziegielewska, K.M., Ek, C.J., Habgood, M.D., Bauer, H., Bauer, H.C., Lindsay, H., Wakefield, M.J., Strazielle, N., Kratzer, I., et al. (2013). Mechanisms that determine the internal environment of the developing brain: a transcriptomic, functional and ultrastructural approach. PLoS ONE *8*, e65629.

Lindahl, P., Johansson, B.R., Levéen, P., and Betsholtz, C. (1997). Pericyte loss and microaneurysm formation in PDGF-B-deficient mice. Science *277*, 242–245.

Lindblom, P., Gerhardt, H., Liebner, S., Abramsson, A., Enge, M., Hellstrom, M., Backstrom, G., Fredriksson, S., Landegren, U., Nystrom, H.C., et al. (2003). Endothelial PDGF-B retention is required for proper investment of pericytes in the microvessel wall. Genes Dev. *17*, 1835–1840.

Louveau, A., Smirnov, I., Keyes, T.J., Eccles, J.D., Rouhani, S.J., Peske, J.D., Derecki, N.C., Castle, D., Mandell, J.W., Lee, K.S., et al. (2015). Structural and functional features of central nervous system lymphatic vessels. Nature *523*, 337–341.

Lunde, L.K., Camassa, L.M., Hoddevik, E.H., Khan, F.H., Ottersen, O.P., Boldt, H.B., and Amiry-Moghaddam, M. (2015). Postnatal development of the molecular complex underlying astrocyte polarization. Brain Struct. Funct. *220*, 2087–2101.

Lundgaard, I., Lu, M.L., Yang, E., Peng, W., Mestre, H., Hitomi, E., Deane, R., and Nedergaard, M. (2017). Glymphatic clearance controls state-dependent changes in brain lactate concentration. J. Cereb. Blood Flow Metab. *37*, 2112–2124.

Lundgaard, I., Wang, W., Eberhardt, A., Vinitsky, H.S., Reeves, B.C., Peng, S., Lou, N., Hussain, R., and Nedergaard, M. (2018). Beneficial effects of low alcohol exposure, but adverse effects of high alcohol intake on glymphatic function. Sci. Rep. *8*, 2246.

Madeira, M.D., Sousa, N., Lima-Andrade, M.T., Calheiros, F., Cadete-Leite, A., and Paula-Barbosa, M.M. (1992). Selective vulnerability of the hippocampal pyramidal neurons to hypothyroidism in male and female rats. J. Comp. Neurol. *322*, 501–518.

Mathiisen, T.M., Lehre, K.P., Danbolt, N.C., and Ottersen, O.P. (2010). The perivascular astroglial sheath provides a complete covering of the brain microvessels: an electron microscopic 3D reconstruction. Glia *58*, 1094–1103.

Mestre, H., Hablitz, L.M., Xavier, A.L., Feng, W., Zou, W., Pu, T., Monai, H., Murlidharan, G., Castellanos Rivera, R.M., Simon, M.J., et al. (2018). Aquaporin-4-dependent glymphatic solute transport in the rodent brain. eLife *7*, e40070.

Mollanji, R., Bozanovic-Sosic, R., Zakharov, A., Makarian, L., and Johnston, M.G. (2002). Blocking cerebrospinal fluid absorption through the cribriform plate increases resting intracranial pressure. Am. J. Physiol. Regul. Integr. Comp. Physiol. *282*, R1593–R1599.

Nagelhus, E.A., and Ottersen, O.P. (2013). Physiological roles of aquaporin-4 in brain. Physiol. Rev. *93*, 1543–1562.

Nagelhus, E.A., Veruki, M.L., Torp, R., Haug, F.M., Laake, J.H., Nielsen, S., Agre, P., and Ottersen, O.P. (1998). Aquaporin-4 water channel protein in the rat retina and optic nerve: polarized expression in Müller cells and fibrous astrocytes. J. Neurosci. *18*, 2506–2519.

Neely, J.D., Amiry-Moghaddam, M., Ottersen, O.P., Froehner, S.C., Agre, P., and Adams, M.E. (2001). Syntrophin-dependent expression and localization of aquaporin-4 water channel protein. Proc. Natl. Acad. Sci. U S A *98*, 14108–14113.

Nevins, T.D., and Kelley, D.H. (2017). Front tracking for quantifying advection-reaction-diffusion. Chaos *27*, 043105.

Nevins, T.D., and Kelley, D.H. (2018). Front tracking velocimetry in advection-reaction-diffusion systems. Chaos *28*, 043122.

Nielsen, S., Nagelhus, E.A., Amiry-Moghaddam, M., Bourque, C., Agre, P., and Ottersen, O.P. (1997). Specialized membrane domains for water transport in glial cells: high-resolution immunogold cytochemistry of aquaporin-4 in rat brain. J. Neurosci. *17*, 171–180.

Peng, W., Achariyar, T.M., Li, B., Liao, Y., Mestre, H., Hitomi, E., Regan, S., Kasper, T., Peng, S., Ding, F., et al. (2016). Suppression of glymphatic fluid transport in a mouse model of Alzheimer's disease. Neurobiol. Dis. *93*, 215–225.

Plog, B.A., and Nedergaard, M. (2018). The glymphatic system in central nervous system health and disease: past, present, and future. Annu. Rev. Pathol. *13*, 379–394.

Rangroo Thrane, V., Thrane, A.S., Plog, B.A., Thiyagarajan, M., Iliff, J.J., Deane, R., Nagelhus, E.A., and Nedergaard, M. (2013). Paravascular microcirculation facilitates rapid lipid transport and astrocyte signaling in the brain. Sci. Rep. *3*, 2582.

Regan, M.R., Huang, Y.H., Kim, Y.S., Dykes-Hoberg, M.I., Jin, L., Watkins, A.M., Bergles, D.E., and Rothstein, J.D. (2007). Variations in promoter activity reveal a differential expression and physiology of glutamate transporters by glia in the developing and mature CNS. J. Neurosci. *27*, 6607–6619.

Ringstad, G., Valnes, L.M., Dale, A.M., Pripp, A.H., Vatnehol, S.S., Emblem, K.E., Mardal, K.A., and Eide, P.K. (2018). Brain-wide glymphatic enhancement and clearance in humans assessed with MRI. JCI Insight *3*, 121537.

Roberts, L.M., Black, D.S., Raman, C., Woodford, K., Zhou, M., Haggerty, J.E., Yan, A.T., Cwirla, S.E., and Grindstaff, K.K. (2008). Subcellular localization of transporters along the rat blood-brain barrier and blood-cerebral-spinal fluid barrier by in vivo biotinylation. Neuroscience *155*, 423–438.

Saunders, N.R., Liddelow, S.A., and Dziegielewska, K.M. (2012). Barrier mechanisms in the developing brain. Front. Pharmacol. *3*, 46.

Saunders, N.R., Habgood, M.D., Møllgård, K., and Dziegielewska, K.M. (2016). The biological significance of brain barrier mechanisms: help or hindrance in drug delivery to the central nervous system? F1000Res. *5*, F1000 Faculty Rev-313.

Schain, A.J., Melo-Carrillo, A., Strassman, A.M., and Burstein, R. (2017). Cortical spreading depression closes paravascular space and impairs glymphatic flow: implications for migraine headache. J. Neurosci. *37*, 2904–2915.

Schreiner, B., Romanelli, E., Liberski, P., Ingold-Heppner, B., Sobottka-Brillout, B., Hartwig, T., Chandrasekar, V., Johannssen, H., Zeilhofer, H.U., Aguzzi, A., et al. (2015). Astrocyte depletion impairs redox homeostasis and triggers neuronal loss in the adult CNS. Cell Rep. *12*, 1377–1384.

Shokri-Kojori, E., Wang, G.J., Wiers, C.E., Demiral, S.B., Guo, M., Kim, S.W., Lindgren, E., Ramirez, V., Zehra, A., Freeman, C., et al. (2018). β-Amyloid accumulation in the human brain after one night of sleep deprivation. Proc. Natl. Acad. Sci. U S A *115*, 4483–4488.

Silver, I., Kim, C., Mollanji, R., and Johnston, M. (2002). Cerebrospinal fluid outflow resistance in sheep: impact of blocking cerebrospinal fluid transport through the cribriform plate. Neuropathol. Appl. Neurobiol. *28*, 67–74.

Sturrock, R.R. (1979). A morphological study of the development of the mouse choroid plexus. J. Anat. *129*, 777–793.

Vanlandewijck, M., He, L., Mäe, M.A., Andrae, J., Ando, K., Del Gaudio, F., Nahar, K., Lebouvier, T., Laviña, B., Gouveia, L., et al. (2018). A molecular atlas of cell types and zonation in the brain vasculature. Nature *554*, 475–480.

Wang, M., Ding, F., Deng, S., Guo, X., Wang, W., Iliff, J.J., and Nedergaard, M. (2017). Focal solute trapping and global glymphatic pathway impairment in a murine model of multiple microinfarcts. J. Neurosci. *37*, 2870–2877.

Wen, H., Nagelhus, E.A., Amiry-Moghaddam, M., Agre, P., Ottersen, O.P., and Nielsen, S. (1999). Ontogeny of water transport in rat brain: postnatal expression of the aquaporin-4 water channel. Eur. J. Neurosci. *11*, 935–945.

Whish, S., Dziegielewska, K.M., Møllgård, K., Noor, N.M., Liddelow, S.A., Habgood, M.D., Richardson, S.J., and Saunders, N.R. (2015). The inner CSF-brain barrier: developmentally controlled access to the brain via intercellular junctions. Front. Neurosci. *9*, 16.

Wolburg, H., Wolburg-Buchholz, K., Fallier-Becker, P., Noell, S., and Mack, A.F. (2011). Structure and functions of aquaporin-4-based orthogonal arrays of particles. Int. Rev. Cell Mol. Biol. *287*, 1–41.

Xavier, A.L.R., Hauglund, N.L., von Holstein-Rathlou, S., Li, Q., Sanggaard, S., Lou, N., Lundgaard, I., and Nedergaard, M. (2018). Cannula implantation into the cisterna magna of rodents. J. Vis. Exp. (*135*), e57378.

Xie, L., Kang, H., Xu, Q., Chen, M.J., Liao, Y., Thiyagarajan, M., O'Donnell, J., Christensen, D.J., Nicholson, C., Iliff, J.J., et al. (2013). Sleep drives metabolite clearance from the adult brain. Science *342*, 373–377.

Xu, Z., Xiao, N., Chen, Y., Huang, H., Marshall, C., Gao, J., Cai, Z., Wu, T., Hu, G., and Xiao, M. (2015). Deletion of aquaporin-4 in APP/PS1 mice exacerbates brain Aβ accumulation and memory deficits. Mol. Neurodegener. *10*, 58.

Zeppenfeld, D.M., Simon, M., Haswell, J.D., D'Abreo, D., Murchison, C., Quinn, J.F., Grafe, M.R., Woltjer, R.L., Kaye, J., and Iliff, J.J. (2017). Association of Perivascular Localization of Aquaporin-4 With Cognition and Alzheimer Disease in Aging Brains. JAMA Neurol. *74*, 91–99.

# STAR★METHODS

## KEY RESOURCES TABLE

| REAGENT or RESOURCE | SOURCE | IDENTIFIER |
|---|---|---|
| Antibodies | | |
| Rabbit polyclonal anti-AQP4 | Merck Millipore | Cat#AB3594; RRID: AB_91530 |
| Mouse monoclonal anti-GLUT1 | Abcam | Cat#MABS132; RRID: AB_2571629 |
| Rat CD140b monoclonal antibody | eBioscience | Cat#14-1402-82; RRID: AB_467493 |
| Donkey anti-Rat Alexa Fluor 488 | Thermofischer | Cat#A-21208; RRID: AB_141709 |
| Donkey anti-Rabbit Alexa Fluor 568 | Thermofischer | Cat#A10042; RRID: AB_2534017 |
| Rabbit anti-human AQP4 | Aviva Systems biology | Cat#OABB01958 |
| Donkey anti-mouse Alexa Fluor 568 | Thermofischer | Cat#A10037; RRID: AB_2534013 |
| Anti-rabbit IgG, HRP-linked antibody | Cell Signaling | Cat#7074; RRID: AB_2099233 |
| Anti-mouse IgG, HRP-linked antibody | Cell signaling | Cat#7076; RRID: AB_330924 |
| Anti-beta-tubulin | Sigma-Aldrich | Cat#T4026; RRID: AB_477577 |
| Chemicals, Peptides, and Recombinant Proteins | | |
| DyLight649 labeled Lycopersicon Esculentum | Vector Labs | Cat#DL-1178 |
| Wheat Germ Agglutinin, Alexa Fluor 594 Conjugate | Thermofischer | Cat#W11262 |
| OA Alexa Fluor 647 conjugate | Thermofischer | Cat#34784 |
| FITC-conjugated lysine-fixable dextran | Thermofischer | Cat#D3306 |
| Critical Commercial Assays | | |
| PIERCE BCA protein assay | Fischer Scientific | Cat#10741395 |
| Experimental Models: Organisms/Strains | | |
| Mouse strain: C57BL/6 | Jackson USA/Taconic Europe | MGI:5656552 |
| Mouse strain: BAC GLT1-eGFP | | MGI:3844618 |
| Mouse strain: *Pdgfb*$^{ret/ret}$ | | MGI:2670572 |
| Software and Algorithms | | |
| FrontTracker.m software | | http://www2.me.rochester.edu/projects/dhkelley-lab/WithFlowRelease.zip |
| ImageJ software v1.48 | NIH | https://imagej.nih.gov/ij/download.html |

## CONTACT FOR REAGENT AND RESOURCE SHARING

Further information and requests for resources and reagents should be directed to and will be fulfilled by the Lead Contact, Iben Lundgaard (iben.lundgaard@med.lu.se).

## EXPERIMENTAL MODEL & SUBJECT DETAILS

Wild-type C57BL/6 mice were purchased from Jackson (USA) or Taconic (Europe) and BAC eGFP-GLT1 mice (Regan et al., 2007) and *Pdgfb*$^{ret/ret}$ mice (Lindblom et al., 2003) were used. Mice were housed according to University of Rochester regulations and compliant with the Association for the Assessment and Accreditation of Laboratory Animal Care (AAALAC) standards. The experiments were approved by University of Rochester Institutional Animal Care and Use Committee. For the experiments carried out at Lund University, all procedures were approved by the local ethical committee for the use of laboratory animals and the Swedish Department of Agriculture (Jordbruksverket). The transgenic mouse strains were backcrossed with C57BL/6 ca. every 9$^{th}$ generation. The mice were kept in a pathogen-free environment with a 12:12 h light/dark cycle, and access to standard diet and water *ad libitum*. Male and female mice were used with a distribution of 45%–55% of each gender in the groups. Some mice were used for E17.5, postnatal day (P) 0-1 (referred to as P1), P 7-8 (referred to as P7), P 14-15 (referred to as P14) or when adult (minimum P56). The weight of the brains was: 156.1 ± 0.008, 390.0 ± 0.01, 486.0 ± 0.008 and 601.4 ± 0.01 mg for P1, P7, P8, P14 and adult mice.

## METHOD DETAILS

### Anesthesia

Since injectable anesthesia is not feasible for newborn mice, isoflurane anesthesia was used for all ages. Anesthesia was induced using 5% isoflurane in 2L/min $O_2$ for neonates and at 2.5% isoflurane in 2L/min $O_2$ for all other postnatal age groups. The maintenance dose was kept between 2%–2.5% isoflurane in 2L/min $O_2$ while closely observing respiration.

### Intracisternal tracer infusion procedure

Alexa-647 conjugated OA (45 kDa, OA-45 kDa, ThermoFischer) and FITC-conjugated lysine-fixable 3 kDa dextran (dextran-3 kDa, ThermoFischer) were used. Tracers were injected in a concentration of 2%. The volumes injected were 1 μL for P1 mice and P7, 2 μL for P14 mice and 5 μL for adult mice. The injection time was 10 min for all mice and rate of injection adjusted accordingly. Mice were anesthetized. An incision in the skin was made to expose the dorsal part of the skull and connective tissue layers were removed to expose the dura covering the cisterna magna. Mice were imaged through intact skull. Intracisternal co-infusion of fluorescent tracers (dextran-3kDa and OA-45kDa) into the cisterna magna was performed with a Harvard apparatus pump using a 50 μl Hamilton syringe with polyethylene tube (I.D. 0.28mm) and a 30G needle. After 60 min circulation time decapitation was performed, followed by quick removal of the brain to be immersion fixed in 4% paraformaldehyde (PFA) overnight.

### Embryonic tracer infusion and imaging

Experiments were performed on E17.5. The pregnant female mouse was anesthetized with isoflurane in 2 L $O_2$/min (5% isoflurane for induction then 2%–3% during the procedure). The body temperature, oxygenation, heart rhythm and temperature (maintained at 37°C) were monitored throughout the procedure to maintain normal blood perfusion to the embryos. A caesarian section was used to expose the embryos. Embryos were kept moist while outside of the abdomen. One at a time embryos were positioned, and the cisterna magna injection site was found using a light source. Freehand injection with a glass needle (80 μm external diameter; 60 μm internal diameter) allowed a total volume of 1μl fluorescent tracer mix into the CSF. The injection rate was 0.1 μL/min. 20min-1hr later the whole embryos were immersion-fixed in 4% PFA and whole embryos and brains of embryos were imaged using an Olympus MVX10 microscope with 0.8X magnification.

### *In vivo* tracer influx imaging

Tracer influx was imaged using an Olympus MVX10 microscope with 1.6X magnification. Images were acquired every minute for a period of 60 minutes using Metamorph Basic software.

### Immunohistochemisty and lectin labeling

Free-floating 100 μm brain sections were blocked for 1hr at room temperature in solution of 7% Donkey Serum and 0.3% Triton in PBS. Primary antibodies (rabbit anti-AQP4, 1:500, MerckMillipore; mouse anti-GLUT1, 1:350, Abcam; rat anti-PDGFRb, 1:100, eBioscience clone APB5) in 1% normal donkey serum and 0.1% triton in PBS were then applied and incubated on a rocking table over night at room temperature. The brain sections were washed in PBS 3x10 min before secondary antibodies (Alexa Fluor 488-, 568- and 647-conjugated secondary antibodies, Thermofischer, 1:500) were applied. Brain slices were incubated for 2 hours on a rocking table at room temperature and washed in PBS before mounting.

Paraffin sections (4 μm thick) were deparaffinized and rehydrated following standard protocols and prepared for immuno-detection of aquaporin-4 (AQP4). After antigen retrieval (10 min. boiling in citrate buffer, pH 6), blocking for endogenous peroxidase activity ($H_2O_2$ for 15 min), and non-specific binding (10% normal goat serum), sections were incubated overnight at 4°C with the primary antibody polyclonal rabbit anti-human AQP4 (Aviva Systems Biology, OABB01958), 1:3000. Primary antibodies were detected by using the DakoCytomation EnVision+DualLink System, Peroxidase (DAB+), code System with peroxidase and DAB (code K5007). Sections were counter-stained with Mayers hematoxylin, dehydrated in graded alcohols and coverslipped with Pertex mounting medium (Liddelow et al., 2013). Control sections in which one of the antibodies was omitted or a non-immune rabbit serum was used always appeared blank. Positive controls included staining of tissue known to be immunoreactive for AQP4, such as kidney.

Evaluation of endfeet was performed on BAC GLT1-eGFP mice (Regan et al., 2007). P1 and P7 mice were anesthetized with 5% isoflurane in 2L/min $O_2$ while P14 and adult mice were anesthetized with ketamine-xylazine (120 mg/mL, 12 mg/mL, intraperitoneally). P1, P7, P15, and adult mice were transcardially perfusion with PBS then 1, 2, 2 and 5 mL of 150 μg/mL AlexaFluor 594-conjugated weat germ agglutinin lectin, respectively. Following the lectin perfusion the mice were perfused with 4% PFA and sectioned in 100μm on a Leica VTS100 vibratome.

Immunohistochemistry and lectin angiography were imaged using a confocal scanning microscope attached to an inverted microscope (IX81, Olympus) controlled by Olympus Fluoview 500 software.

### Isolation of cerebral blood vessels

All steps were carried out on ice or at 4°C. Cortices and hippocampi were dissected from freshly isolated brains in HBSS buffer containing 20 mM HEPES (pH 7.4). Cerebral cortices and hippocampi were minced with a razor blade and homogenized by multiple strokes of a 10 mL syringe with a spinal needle (25G) for 60 s. Homogenate from each rat brain tissue was centrifuged at 2000 × g for

10 min, and the cloudy supernatant was collected as a parenchymal homogenate. The loose pellet was resuspended in 18% 500 kDa dextran (T-500, Pharmacia) in HBSS buffer containing 20 mM HEPES and centrifuged at 4,400 × g for 15 min. The resulting floating myelin-rich layer and dextran supernatant were decanted, the inside wall of the tube was blotted with an absorbent paper to remove all residual fluids and the microvessel pellet was resuspended in HBSS containing 20 mM HEPES. The previously isolated parenchymal supernatant was then centrifuged at 4,400 × g for 15 min at 4°C and the vessel pellet was mechanically grinded using a Micro-tissue grinder (Carl Roth) during multiple freeze-thaw cycles and underwent a third centrifugation at 4,400 × g for 10 min at 4°C and microvessel pellets were stored at −80°C until used for protein extraction. For adult mice, one brain per sample was used, and minimum 3 brains were pooled to yield one sample of P14, P7, P1 mice.

### Western blotting

Protein concentration was determined by PIERCE BCA protein assay (Fisher Scientific). Samples were heated for 10 min at 95°C in sample buffer (2.0ml 1M Tris-HCl, pH 6.8, 2% SDS, 10% glycerol, 1% 14.7 M β-mercaptoethanol 12.5mM EDTA, 0.02% bromophenol blue). Proteins were then separated on 12% Bis-acrylamid mini gels containing 0.1% 2,2,2-Trichloroethanol for subsequent visualization of protein loading using a Chemidoc MP imaging system (Biorad). Following protein transfer onto PVDF membranes (Biorad), transfer efficiency was checked using a Chemidoc MP imaging system (Biorad). The membranes were blocked for 60 min in 1% bovine serum albumin (in phosphate-buffered saline containing 1% Tween 20 (PBST); 137mM NaCl, 2.7mM KCl, 10mM Na2HPO4, 1.76mM K2HPO4; pH 7.4) and sequentially incubated with the primary and secondary antibodies. A 1:1000 dilution for the primary antibody (rabbit anti-AQP4, Chemicon, as used for immunostainings; mouse anti-β-tubulin, Sigma Aldrich), and 1:10,000 for the HRP-labeled secondary antibody (anti-rabbit and anti-mouse IgG, Cell Signaling) were utilized. All antibodies were diluted in 1% bovine serum albumin in PBST.

## QUANTIFICATION AND STATISTICAL ANALYSES

### AQP4 polarization analysis

The polarization of AQP4 along vessels in tissue was quantified in cortex and hippocampus (Kress et al., 2014; Lundgaard et al., 2018). Blood vessels were selected at random on confocal images and marked cross-sectionally using the line plot tool in ImageJ to include AQP4 signal from vascular endfeet and from the surrounding parenchyma. The average vessel to average parenchyma fluorescence intensity ratio was used as a measure of AQP4 vascular polarization to vascular endfeet. The polarization was also measured using western blotting of vascular isolations.

### *In vivo* tracer influx quantification

Quantification of the influx into different regions was done with ImageJ software. The mean fluorescence intensity was measured for the regions of interest (ROI), including cortex, hindbrain in P1 or cerebellum in P7 and older, and olfactory bulb. Mean fluorescent pixel intensities in ROIs were normalized to the area with the highest mean fluorescence intensity for each animal.

### Western blotting

A standard chemiluminescence procedure (ECL Plus) was used to visualize protein binding using a Chemidoc MP imaging system (Biorad). The images were evaluated densitometrically using ImageJ software (1.48v).

### Tracer influx tracking

At the magnifications used in this study, regions of high tracer concentration and regions of low tracer concentration are separated by sharp boundaries. The motion of these concentration fronts indicates the motion of tracer at the pial surface. Fronts were tracked using FrontTracker.m, a MATLAB function described previously (Nevins and Kelley, 2017). The function locates fronts according to a user-defined intensity threshold, applying spatial smoothing to offset imprecision due to pixelization. The function then measures the local velocity of each front at many points along the front (one measurement per pixel) by determining the perpendicular distance over which the front advances between subsequent images. Front velocity measurements are robust to variation in user parameters, including intensity threshold, especially when fronts are sharp (Nevins and Kelley, 2017). Though the function is capable of separating the effects of bulk flow from those of diffusion and reaction (Nevins and Kelley, 2018), that capability is unnecessary here: front velocities described in this paper are the net result of the combined effects of bulk flow, diffusion, and reaction (though reaction probably has negligible effects over these timescales).

### Statistics

For pairwise comparisons a Student's t test were used. Multiple groups were analyzed using a one-way ANOVA analysis with Dunnett tests. For two independent variables 2-way ANOVA with Tukey test was used. Probability values $< 0.05$ were deemed significant. For both pericyte count and AQP4 polarization a one-way ANOVA with Tukey test was used. Mean AQP4 intensity and pericyte-blood vessel association were analyzed using a Kruskal-Wallis with Dunn's Test. All values are expressed as mean ± SEM. Specific statistical tests used for each figure are available in the corresponding figure legend. Capital "N" represents number of animals. Lowercase "n" represents number of samples, with an equal number of samples from each animal and a minimum number of 3 animals used.

**Cell Reports, Volume *26***

## Supplemental Information

# PDGF-B Is Required for Development of the Glymphatic System

**Anne Sofie Munk, Wei Wang, Nicholas Burdon Bèchet, Ahmed M. Eltanahy, Anne Xiaoan Cheng, Björn Sigurdsson, Abdellatif Benraiss, Maarja A. Mäe, Benjamin Travis Kress, Douglas H. Kelley, Christer Betsholtz, Kjeld Møllgård, Anja Meissner, Maiken Nedergaard, and Iben Lundgaard**

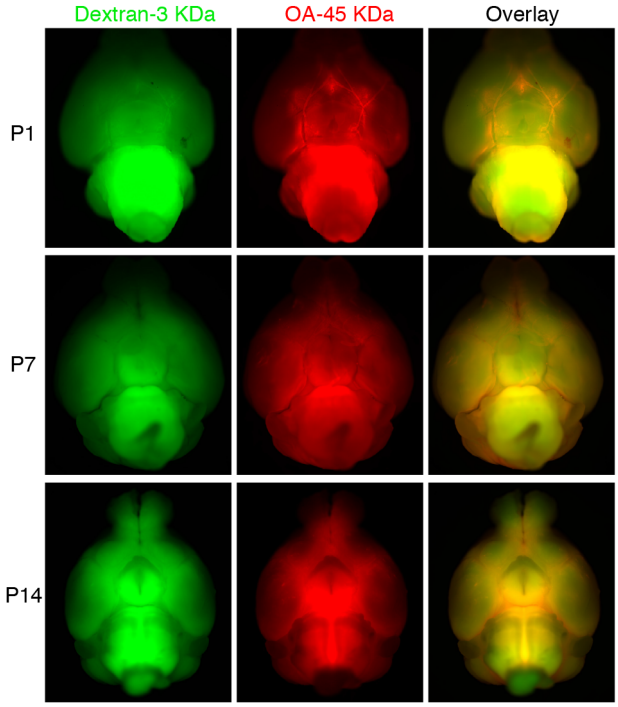


**Figure S1. Ventral view of tracer influx in P1, P7 and P14 mice, Related to Figure 1**

Dorsal view of whole brains showing distribution of CSF tracers FITC-dextran (dextran-3 kDa) and ovalbumin-Alexa647 (OA-45 kDa) 60 min after injection into the cisterna magna. P1 mouse brain (top panel) shows distribution of tracers around the Circle of Willis and along the proximal part of the middle cerebral artery (MCA). Images of dextran-3 kDa and OA-45kDa tracers in P7 (middle panel) and P14 brain (bottom panel) show tracer distribution around the Circle of Willis and the MCAs.

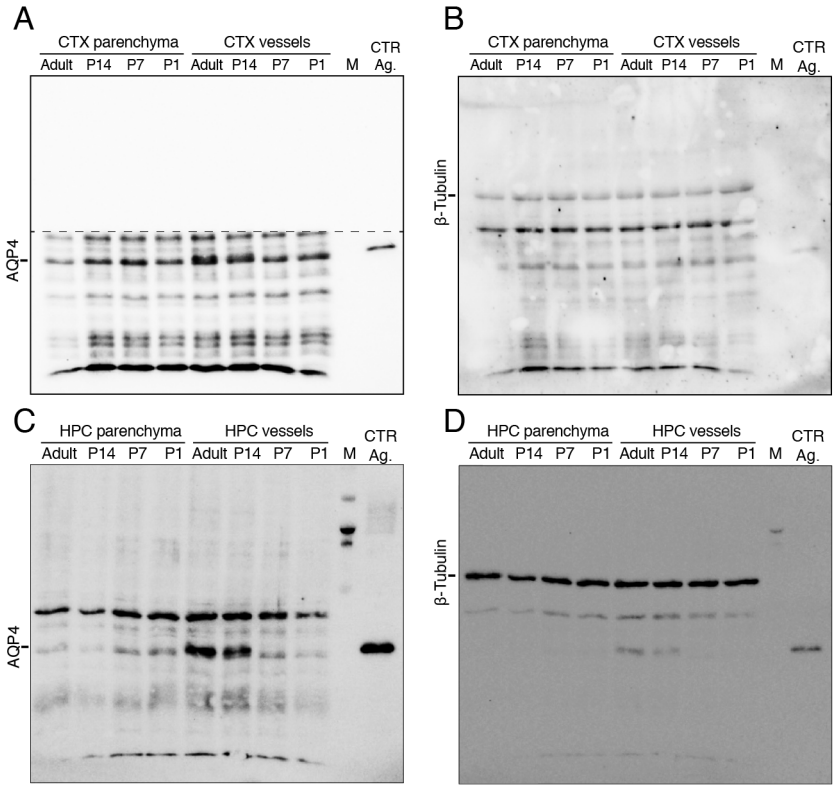


**Figure S2. Western blots of AQP4 vessel – and parenchymal fractions during development, Related to Figure 3**

**A-D**) Representative Western blots of parenchyma fractions and isolated vessel fractions incubated with primary antibodies against aquaporin 4 (AQP4, 38 kDa); and β-tubulin (52 kDa). **A**) The blot was covered starting from the dotted line and upwards to avoid strong signal from off-target bands. CTX, cortex; HPC, hippocampus; P, postnatal day; M, protein marker; CTR Ag., AQP4 control antigen.

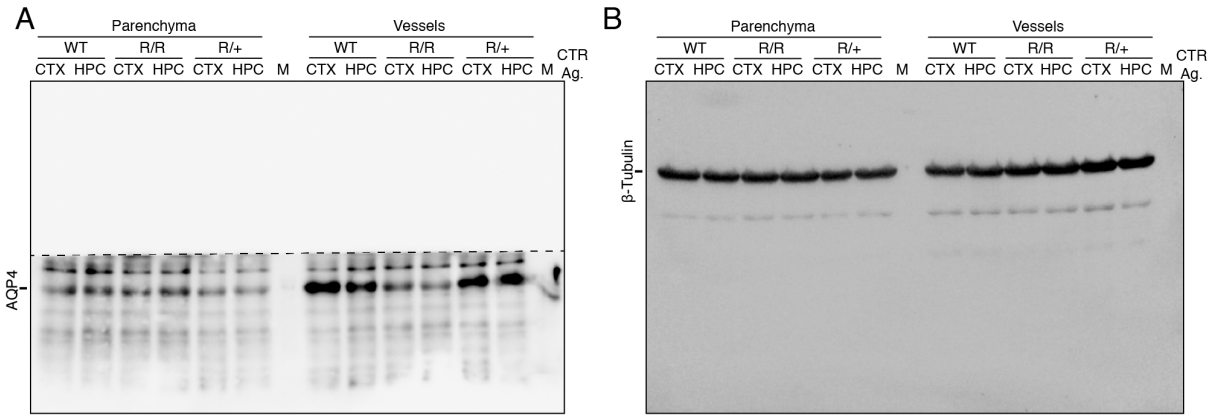


**Figure S3. Western blots of AQP4 vessel – and parenchymal fractions from *Pdgfb*$^{ret/ret}$ mice, Related to Figure 6**

**A-B**) Representative Western blots of parenchyma fractions and isolated vessel fractions incubated with primary antibodies against aquaporin 4 (AQP4, 38 kDa); and β-tubulin (52 kDa). **A**) The blot was covered starting from the dotted line and upwards to avoid strong signal from off-target bands. CTX, cortex; HPC, hippocampus; M, protein marker; CTR Ag., AQP4 control antigen; WT, wild type; R/R, *Pdgfb*$^{ret/ret}$; R/+, *Pdgfb*$^{ret/wt}$.